Journal of
Composites Science

MDPI

Article

Development and Evaluation of a Novel Method for Reinforcing Additively Manufactured Polymer Structures with Continuous Fiber Composites

Sven Meißner [1,*], Jiri Kafka [1], Hannah Isermann [2], Susanna Labisch [2], Antonia Kesel [2], Oliver Eberhardt [3], Harald Kuolt [3], Sebastian Scholz [1], Daniel Kalisch [1], Sascha Müller [4], Axel Spickenheuer [5] and Lothar Kroll [4]

[1] Fraunhofer Plastics Technology Center Oberlausitz, Fraunhofer Institute for Machine Tools and Forming Technology IWU, Theodor-Koerner-Allee 6, 02763 Zittau, Germany; jiri.kafka@iwu.fraunhofer.de (J.K.); sebastian.scholz@iwu.fraunhofer.de (S.S.); daniel.kalisch@iwu.fraunhofer.de (D.K.)
[2] Biomimetics-Innovation-Centre (B-I-C), University of Applied Sciences Bremen, Neustadtswall 30, 28199 Bremen, Germany; hannah.isermann@gmx.de (H.I.); slabisch@bionik.hs-bremen.de (S.L.); akesel@bionik.hs-bremen.de (A.K.)
[3] J. Schmalz GmbH, Johannes-Schmalz-Str. 1, 72293 Glatten, Germany; harald.kuolt@schmalz.de (H.K.)
[4] Department of Lightweight Structures and Polymer Technology, Faculty of Mechanical Engineering, Chemnitz University of Technology, 09111 Chemnitz, Germany; sascha.mueller@mb.tu-chemnitz.de (S.M.); lothar.kroll@mb.tu-chemnitz.de (L.K.)
[5] Mechanics and Composite Materials Department, Leibniz-Institut für Polymerforschung Dresden e. V., Hohe Str. 6, 01069 Dresden, Germany; spickenheuer@ipfdd.de
* Correspondence: sven.meissner@iwu.fraunhofer.de

Abstract: Additively manufactured polymer structures often exhibit strong anisotropies due to their layered composition. Although existing methods in additive manufacturing (AM) for improving the mechanical properties are available, they usually do not eliminate the high degree of structural anisotropy. Existing methods for continuous fiber (cF) reinforcement in AM can significantly increase the mechanical properties in the strand direction, but often do not improve the interlaminar strength between the layers. In addition, it is mostly not possible to deposit cFs three-dimensionally and curved (variable–axial) and, thus, in a path that is suitable for the load case requirements. There is a need for AM methods and design approaches that enable cF reinforcements in a variable–axial way, independently of the AM mounting direction. Therefore, a novel two-stage method is proposed in which the process steps of AM and cF integration are decoupled from each other. This study presents the development and validation of the method. It was first investigated at the specimen level, where a significant improvement in the mechanical properties was achieved compared to unreinforced polymer structures. The Young's modulus and tensile strength were increased by factors of 9.1 and 2.7, respectively. In addition, the design guidelines were derived based on sample structures, and the feasibility of the method was demonstrated on complex cantilevers.

Keywords: additive manufacturing; pultrusion; continuous fiber; structural optimization; lightweight design; fused filament fabrication; fiber-reinforced polymer; thermoplastic polymer; thermoset polymer

Citation: Meißner, S.; Kafka, J.; Isermann, H.; Labisch, S.; Kesel, A.; Eberhardt, O.; Kuolt, H.; Scholz, S.; Kalisch, D.; Müller, S.; et al. Development and Evaluation of a Novel Method for Reinforcing Additively Manufactured Polymer Structures with Continuous Fiber Composites. *J. Compos. Sci.* **2024**, *8*, 272. https://doi.org/10.3390/jcs8070272

Academic Editor: Yuan Chen

Received: 24 June 2024
Revised: 8 July 2024
Accepted: 12 July 2024
Published: 14 July 2024

1. Introduction

AM has gained significant importance in recent years and has now found broad applications in various industries such as mechanical engineering, the automotive industry, aerospace industry, medical industry, and consumer goods production. Compared to conventional manufacturing processes, AM offers the ability to produce components quickly and individually. The resulting flexibility in production allows companies to quickly respond to customer demands and market developments. Additionally, AM enables the realization of complex geometries and shapes that are difficult or even impossible to produce with other manufacturing methods. Furthermore, AM allows for a more efficient

utilization of resources and materials [1]. These advantages have led to the development of numerous AM technologies, which are now utilized throughout the entire value chain, including upstream and downstream processes [2].

While AM offers many advantages, there are deficiencies in the mechanical properties of additively manufactured polymer components. In the AM process, the material is deposited layer by layer, which can lead to a weaker interface between individual layers. This leads to an attenuation of the structure in the mounting direction [3]. As a result, anisotropies can occur in additively manufactured components, whereas conventional polymer processing/manufacturing methods (such as unreinforced injection molding) typically achieve nearly isotropic structures. Therefore, additively manufactured structures generally cannot exhibit the same mechanical properties as components produced with the same material using conventional manufacturing processes.

Intensive research has been and is being conducted to improve the mechanical properties of additively manufactured polymer components. Specifically tailored materials were developed for AM, which exhibit a higher strength and durability, for example, by influencing the rheology through the compounding with additives [4–7]. Efforts also been made to optimize the AM processes to achieve better interfaces between the layers, such as through temperature control of the build chamber and build platform, as well as adjustments to the extrusion temperature or layer thickness [8–11]. Post-processing steps such as annealing are also considered to enhance the mechanical properties of the components [12]. Overall, addressing the deficiencies in the mechanical properties is an important area of research to further optimize AM and expand its application scope.

To overcome the deficiencies of a pure, unreinforced polymer in terms of its low mechanical properties, short fibers are often added to the polymer for structural reinforcement. For example, in Selective Laser Sintering (SLS), short fibers are mixed with the polymer powder [13–16], while in Fused Filament Fabrication (FFF), short fibers are added to the filament or granulate [16–19]. Short fibers offer the advantage of being relatively easy to process, increasing the mechanical properties in the direction of the fiber alignment, and significantly reducing part warping and distortion. However, compounding with short fibers does not contribute to an improvement in layer adhesion and therefore does not lead to a significant increase in the mechanical properties of additively manufactured polymer structures in the mounting direction.

The mechanical deficiencies prevent the realization of some applications, particularly mechanically highly stressed structures [20]. Therefore, enhancing the mechanical properties can help to expand the range of applications for AM to further increase the already high potential of AM. An improvement in the mechanical properties can be achieved, particularly through the integration of cFs. AM processes utilizing cFs can achieve comparable tensile strengths to conventionally manufactured fiber-reinforced polymer (FRP) structures [21]. Continuous carbon fibers are predestined, as they offer an exceedingly high Young's modulus as well as specific tensile strength compared to glass or Kevlar fibers, for example.

Figure 1 illustrates AM methods in which cFs are processed for component reinforcement. There is a possible classification according to the time and place of contact between the fibers and the melt [22]. The filament extrusion process uses cF-reinforced thermoplastic pre-impregnated filaments, known as towpregs. During extrusion, the towpreg is heated in the print head, the matrix is melted, and then, it is deposited layer by layer [23,24]. At the in situ impregnation process, dry cFs and a polymer filament are introduced separately into the print head. By heating, the polymer is melted, the cFs are impregnated, and then, they are deposited on the build platform [12,24]. In the dual extrusion process, a cF towpreg and a thermoplastic filament are deposited on the build platform through separate print heads [12,24]. The in situ co-extrusion process is characterized by the separate supply of the polymer filament and towpreg to the print head. In the print head, the towpreg is impregnated with the polymer matrix [25]. In situ consolidation is a scaled-down version of an Automated Tape Laying (ATL) process for thermoplastics. Pre-made towpregs or

prepreg tapes are consolidated during and after deposition by applying heat [26]. At inline impregnation, dry fibers are pre-impregnated outside the print head, then transported into the print head and subsequently deposited [22].

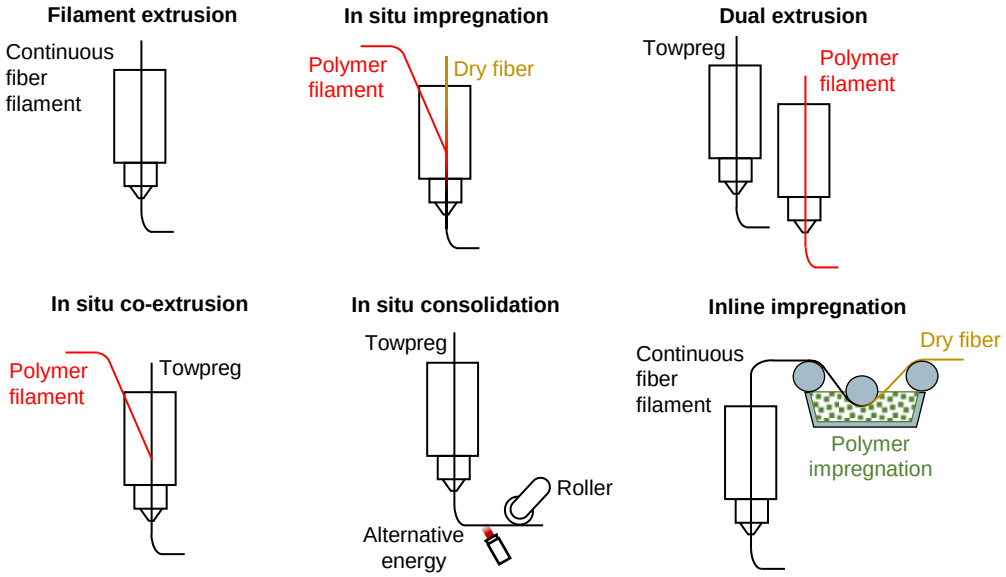

Figure 1. Technologies for AM with cF reinforcement, inspired by [22].

The described cF-AM methods deposit the fibers during the AM process mainly parallel to an even building plate. The in-plane deposition does not allow for the orientation of reinforcing material in a three-dimensional direction. Additionally, the deficiency of the layer interface strength in the mounting direction could not be improved either. There is a need for AM methods and design approaches that enable cF composite reinforcements in a three-dimensional curved (variable–axial) way, independently of the AM mounting direction. A variable–axial orientation of the reinforcement fibers offers the advantage that mechanical loads result in a more uniform distribution of stresses among the reinforcement fibers, while the matrix material is subjected to lower stresses. The high specific stiffness and strength of the fiber materials can consequently be optimally utilized. A significant reduction in material usage and an increase in lightweight construction are demonstrated by existing FRP processes that enable variable–axial fiber orientations (e.g., Tailored Fiber Placement), in contrast to conventional processes with multi-axial layering [27]. In AM, two-stage manufacturing processes have the potential to meet this demand by decoupling the integration of a continuous fiber-reinforced polymer (cFRP) from the AM process. One example is composite structures, where thermoplastic pre-impregnated unidirectional tapes are melted onto a polymer basic structure fabricated using an extrusion-based AM process [28,29].

The objective of this research is to develop and evaluate a novel two-stage method for reinforcing additively manufactured polymer structures with a cFRP. The approach decouples the process steps AM and cF implementation by inserting cFRP structures into component-integrated channels of an additively manufactured polymer's basic structure. The orientation of the integrated cFRP structures into the additively manufactured polymer structure corresponds to the principal stress lines of the load-bearing structure. The basic component design, which is initially based on classical topology optimization, is supplemented by a load-adapted, variable–axial orientation of the reinforcing fibers within the additively manufactured polymer structure.

The approach is mostly unexplored and distinguished by a high degree of novelty. This study presents the investigations on the feasibility of the method, as well as on the material characterization and the development of general design guidelines. In addition, a demonstrative implementation is intended. For the design of the demonstrators, a

numerical tool will be developed to optimize the arrangement and orientation of the component-integrated cFRP. The demonstrators will be manufactured and analyzed, and potential improvements for the novel method will be derived.

2. Materials and Methods

The research program for the development and validation of the novel method is shown in Figure 2. The investigations start at the specimen level. The level of geometric complexity of the sample structures is subsequently increased, and finally, a proof of concept is provided by means of demonstrators.

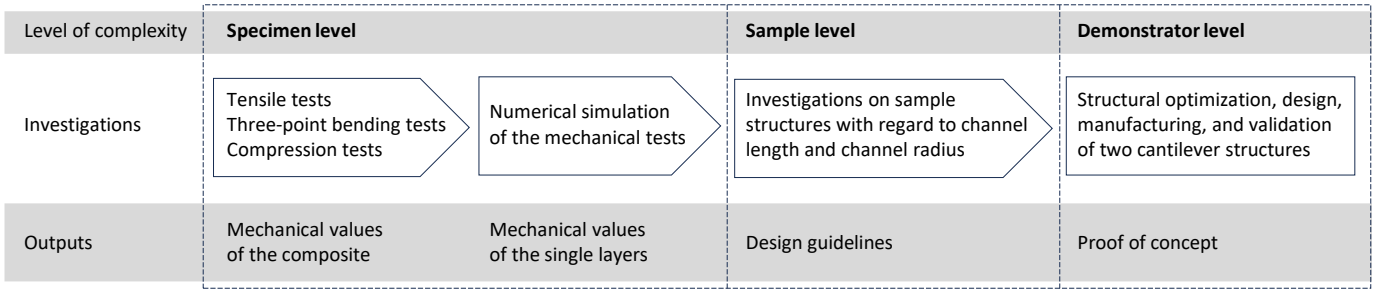

Figure 2. Research program for the development and validation of the novel method.

2.1. Manufacturing Method

The novel method was realized by using the manufacturing steps shown in Figure 3. First, a basic polymer structure is additively manufactured. In the basic structure, component-integrated channels are included. cF bundles are impregnated with a polymer matrix by passing them through a resin bath filled with liquid matrix material. The impregnated cF bundles are pulled through the component-integrated channels of the additively manufactured basic structure by using a traction rope. This pultrusion process enables a high fiber-volume ratio (FVR) to be realized. The matrix of the impregnated cF bundles cross-links within the component and forms a solid FRP with the additively manufactured basic structure.

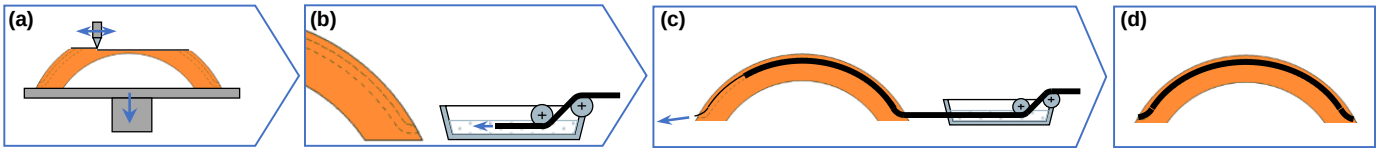

Figure 3. Process principle of the novel method for reinforcing additively manufactured polymer structures with cFRP. (**a**) AM of polymer basic structure. (**b**) cF impregnation by pulling a cF bundle through a resin bath. (**c**) Pulling impregnated cF bundles through component-integrated channels of the additively manufactured basic structure. (**d**) Cross-linking of the matrix.

The described process was implemented on a laboratory scale and applied to produce each of the specimens, sample components, and demonstrator structures described in this study. In this laboratory process, the fiber bundles were manually pulled through the resin bath and the additively manufactured channel structures using a wire.

2.2. Materials and Process Parameters

The objective of the study is to demonstrate the general feasibility of the two-stage method described. To this purpose, material components are selected, which are versatile and already established in AM as well as in cFRP fabrication and offer a good processability in the respective sub-processes. In addition, the focus in this phase of research with a low technology readiness level is on the use of materials that are available to a wide range of users.

Fused deposition modeling (FDM) by the 3D printing machine Stratasys Fortus 900mc, utilizing acrylonitrile butadiene styrene (ABS-M30-black from the company Stratasys,

Eden Prairie, MN, USA) was used to fabricate the basic polymer structures. All samples were printed with a layer height of 0.254 mm. The temperature of the installation chamber was 95 °C, and the nozzle temperature was 320 °C. The CAD files were exported in STL format and processed using the slicer software Insight 18.6 using single contour and +45°/−45° solid rasters, which are typical default settings.

cFs of type HTS40 from the company Toho Tenax, Chiyoda, Japan, were used as reinforcing fibers. The epoxy resin L + hardener EPH 161 with a viscosity of 560 ± 100 mPa·s from the company R&G, Waldenbuch, Germany, was selected for impregnating the cFs. The fiber impregnation and manually pultrusion process were performed at 20 °C. After the pultrusion, all samples were stored at 20 °C for 24 h, then treated at 60 °C for 15 h and stored again at 20 °C for at least 48 h.

Sufficient adhesion between the ABS structure and the cF-reinforced epoxy can be assumed [30] for the proof of concept according to the objective of the study. A detailed adaptation of the single material components is not the focus of the study. Further investigations regarding material modifications or substitutions should be expanded in further studies.

2.3. Specimen Geometry and Mechanical Tests

Tensile, compression, and flexure specimens were designed in accordance with the current polymer testing standards with production-related adaptations (Figure 4). In each case, the channel shape was selected in a drop shape to eliminate the need for an internal supporting structure in AM. Reinforced specimens with a channel diameter of 5 mm each were manufactured, and the cFRPs were inserted with FVRs φ_{FRP} of 41% and 57%, respectively. The unreinforced specimens had the same outer contour as the reinforced specimens, but the cross-section was closed (without channel). The mechanical tests were carried out with the Zwick/Roell Inspekt 100 kN universal testing device at 23 ± 2 °C and 50 ± 10% rH. The tensile tests were performed in accordance with the ISO 527-4 standard [31]. The speed of testing was 1 mm/min up to 0.3% and 10 mm/min after 0.3% elongation. The three-point bending tests were carried out according to the EN ISO 14125 standard [32]. The span was 80 mm, and the speed of testing 1 mm/min. The compression tests were in accordance with the EN ISO 14126 standard [33] method 1. The speed of testing was 1 mm/min. The material constants listed in Table 1 were extracted from the mechanical tests.

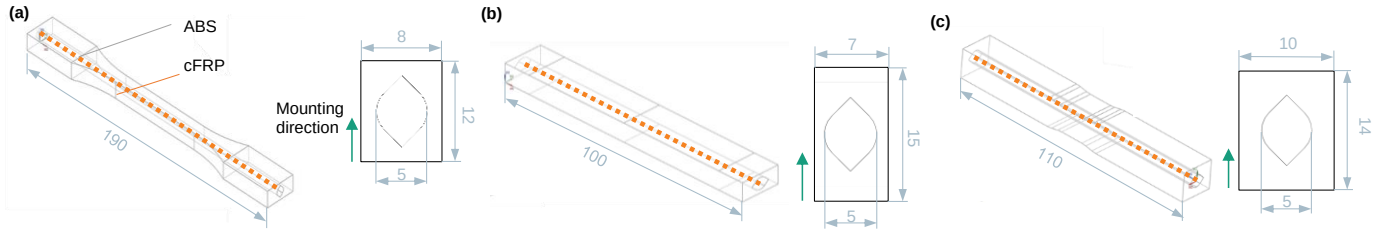

Figure 4. Reinforced specimens for determining mechanical properties consisting of additively manufactured basic structure (ABS) and cross-sectional geometry in the measuring area with drop-shaped channel for integration of cFRP (cF + epoxy). (**a**) Tensile specimen based on ISO 527-2 standard [34] type 1B. (**b**) Three-point bending specimen based on EN ISO 14125 standard. (**c**) Compression specimen based on EN ISO 14126 standard.

Table 1. Determined material constants for unreinforced specimens and reinforced specimens considering two different FVRs.

Tensile test	E:	Young's modulus	σ_m:	Tensile strength at initial failure
Three-point bending test	E_r:	Flexural modulus	σ_f:	Flexural strength at initial failure
Compression test	E_c:	Chord modulus	σ_c:	Compressive strength at initial failure

2.4. Application Scenario for Demonstrator Implementation

The application scenario is selected by the fact that it exhibits a highly loaded supporting structure and requires a high degree of lightweight construction as well as a significant need for customization. Horizontal cantilevers of an ergonomic handling system (Figure 5) [35] are selected for this purpose.

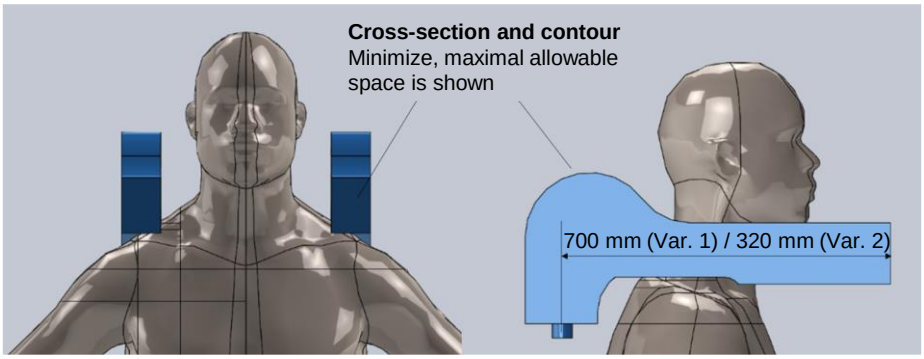

Figure 5. Maximal design space and placement for the "horizontal cantilever", that is, the main part of the planned exoskeleton.

2.5. Numerical Tool for Structure Optimization

The numerical optimization (in the context of the study, the term "optimization" is considered to describe the search for the optimum as well as the process of approximation based on the guideline VDI 6220 Sheet 2: Biomimetics–Biomimetic design methodology–Products and processes) was based on the finite element analysis (FEA) program MARC from Hexagon, release 2023.1, and used the interfaces offered there for data input and output. The control program was programmed in Python, release 3.8. The functionality of this control program BOT (Biomimetic Optimization Tool) is described below.

Two different bio-inspired optimization methods were used for the numerical component optimization, which are particularly effective in terms of lightweight construction optimization [36].

2.5.1. Topology Optimization via SKO

The "Soft Kill Option (SKO)" method was used for topology optimization [37]. In the SKO method, the Young's modulus of each element is varied based on a comparison of the local stress with the reference stress; see Equation (1). The optimization process is divided into several iterations with a linear increase in the reference stress σ_{ref}, each of which consists of several sub-iterations with a constant reference stress. The number of iterations and sub-iterations is determined in advance by the user.

The Young's modulus E of the iteration step $i + 1$ is determined using the following rule:

$$E_{i+1} = E_{max} \cdot \left(\frac{E_i}{E_{max}} + c \cdot \left(\frac{\sigma_i}{\sigma_{ref}} - 1 \right) \right). \quad (1)$$

Here, c is a constant factor, and σ_i is the von Mises yield criterion in the respective element. This update rule is normalized with the maximum Young's modulus E_{max} following Equation (2):

$$E_{i+1} = E_i + \mathrm{k} \cdot (\sigma_\mathrm{i} - \sigma_\mathrm{ref}), \quad (2)$$

with

$$k = c \cdot \frac{E_{max}}{\sigma_{ref}}. \quad (3)$$

As suggested by Baumgartner et al. [38], the normalization provides independence from the magnitude of Young's modulus and the load, so that the result is independent of the units used.

To reduce the computing costs, Young's modulus was cut to the range $E_{max}/1000 \leq E \leq E_{max}$ and rounded to 10 discrete, equidistant elastic modulus gradations. The design proposal resulting from the optimization is made visible at the end by hiding all elements with the low Young's modulus $E = E_{max}/1000$.

Preliminary tests also showed that the usability of the optimization results can be improved by homogenizing the stresses of the individual elements using a moving average. This was achieved using a nearest neighbors algorithm by averaging the stress for each element with the stresses of the k-nearest neighbor elements. The number of neighbor elements determines the resulting structure width of the optimization results.

2.5.2. Fiber Orientation Optimization via CAIO

The second biomimetic optimization method implemented here is the "Computer-Aided Internal Optimization (CAIO)" method, which is used for load-appropriate fiber orientation in the component [39].

The CAIO method, like the SKO method, is an iterative optimization method that is carried out using the finite element analysis. The direction-dependent or orthotropic properties of each element are realigned in each iteration based on the local stress tensor in the major principal direction. The major principal direction is the eigenvector associated with the maximum absolute eigenvalue of the stress tensor of each element.

An implemented further development of the CAIO is the determination of tensile and compressive areas for appropriate material allocation. In each iteration, the tensile and compressive areas were identified in the fiber material, and the respective material parameters were assigned for the next iteration.

In addition to the separate topology and fiber orientation, the two optimization methods (SKO and CAIO) were programmed as a combined method based on the program blocks of both methods (Figure 6). In each iteration step, the updates of both methods are performed on the same model. This requires minor adaptations in the SKO method: To account for the orthotropic material properties during SKO, only Young's modulus in fiber direction E_x was used in the update rule (Section 2.5.1, Equation (1)). As in the pure SKO method, 10 discrete materials were used. As material properties, the Young's moduli in all directions $i \in \{x, y, z\}$ were interpolated towards $E_i = \min\left(E_x, E_y, E_z\right)/1000$, meaning that the material with the minimum Young's modulus has isotropic material properties and, thus, saves computing time during the CAIO part, as no fiber realignment is performed in this regions. Despite the orthotropic material properties, the von Mises stress was chosen as the characteristic stress σ for the material variation during SKO:

$$\sigma = \sqrt{\frac{1}{2}\left[(\sigma_I - \sigma_{II})^2 + (\sigma_{II} - \sigma_{III})^2 + (\sigma_{III} - \sigma_I)^2\right]} \tag{4}$$

with the principal stresses σ_I, σ_{II}, and σ_{III}.

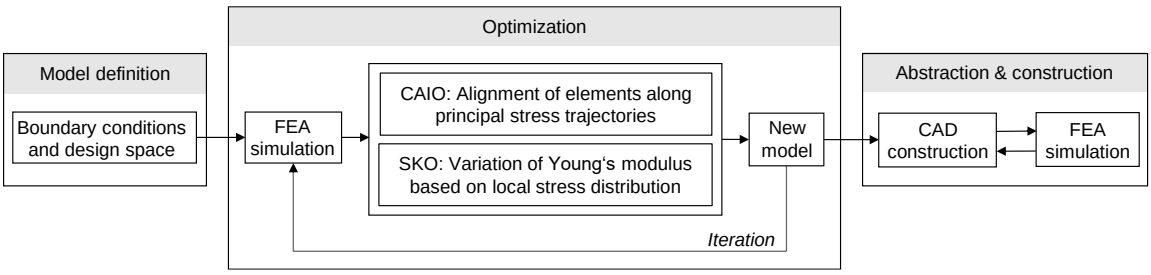

Figure 6. Workflow for the numerical tool used. Presetting of calculation steps and manual selection of a realizable model/geometry.

Element alignment is carried out according to the unmodified CAIO method, which also takes the various compressive and tensile properties of the material into account and assigns the material accordingly.

2.5.3. Component Design

The first step in creating the finite element model was to define a geometry with the maximum permissible installation space in a common CAD system (here: Autodesk Inventor Professional 2021). The geometry was loaded into the preprocessor and meshed there with four-node linear isoparametric tetrahedron elements using linear interpolation functions, resulting in 212,404 elements and 40,641 nodes (Figure 7). The material properties were applied according to the results of material characterization (Section 3.2.5) using the anisotropic mechanical values of the cFRP for tension and compression. The boundary conditions were applied with point loads on 78 nodes on the tip of the cantilever, resulting in a total load of −257.75 N in the x- and y-directions, respectively, and a fixation at the base.

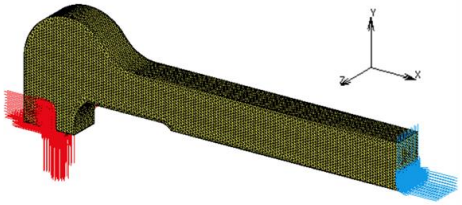

Figure 7. FEA model (here: for the 700 mm long component) defining the construction space with applied boundary conditions; in red, the fixed displacements; and in blue, the applied point loads.

The load shall be transferred to the cantilever arm via a cable pull and a deflection roller. Hence, it was applied in negative x- and y-directions (Figure 7). Besides the 700 mm cantilever, a short component of 320 mm was also realized. Both cantilevers have the same materials and loading.

Finally, the created FEA models were exported for the finite element simulation and optimization with BOT.

2.5.4. FEA Validation of the CAD Construction

In order to validate the generated CAD models, the numerical tool for fiber orientation was extended so that it could implement a specified fiber orientation along the fiber-carrying channels. This has the advantage that compressive- and tension-dominated areas can still be identified, and the corresponding elements can be assigned the compressive or tensile modulus. The material property of the surrounding channel forming matrix was chosen according to the experimentally determined mechanical values in Section 3.2.5. Both demonstrator models, the long version (700 mm) and the short one (320 mm), were loaded in the same way.

3. Results

3.1. Theoretical Considerations on Tensile Behavior

A forecast is made to determine what mechanical properties could theoretically be expected. To calculate the effective FVR and effective Young's modulus, all material components (additively manufactured polymer, cF, and matrix phase) must be considered. The effective FVRs (Table 2) of the specimens (Figure 4) in the measuring range are calculated by

$$\varphi_{eff} = \varphi_{FRP} \cdot A_{FRP} / A_{eff}. \quad (5)$$

The Young's modulus of the cFRP (consisting of cF and matrix phase) is derived by

$$E_{FRP} = \varphi_{FRP} \cdot E_{cF} + (1 - \varphi_{FRP}) \cdot E_{Epoxy}. \quad (6)$$

The theoretically expected effective Young's modulus of the total composite (consisting of the additively manufactured polymer and cFRP phase) in the measuring range is calculated by

$$E_{theor} = \frac{1}{A_{eff}} \cdot \left(E_{FRP} \cdot A_{FRP} + E_{ABS} \cdot \left(A_{eff} \cdot A_{FRP} \right) \right). \quad (7)$$

Table 2. Determination of the effective FVR φ_{eff} of the respective specimen in the measuring range (contains additively manufactured polymer and cFRP phase) according to Equation (5), with A_{FRP}—cross-sectional area of drop-shaped channel, A_{eff}—overall cross-sectional area of the respective specimen in the measuring range, and φ_{FRP}—FVR of the integrated cFRP (contains cF and matrix phase).

Specimen	A_{FRP} [mm²]	A_{eff} [mm²]	φ_{FRP}	φ_{eff}	φ_{FRP}	φ_{eff}
Tension	22.2	96.0	41%	9.5%	57%	13.2%
Flexure		105.0		8.7%		12.0%
Compression		140.0		6.5%		9.0%

The theoretical preliminary considerations in Table 3 show that an increase in stiffness by a factor of 10.5 or 14.1 can be expected compared to an unreinforced additively manufactured polymer.

Table 3. Determination of the theoretically expected Young's moduli E_{theor} of the total composite (contains additively manufactured polymer and cFRP phase) according to Equations (6) and (7), with A_{FRP}—cross-sectional area of drop-shaped channel, A_{eff} —overall cross-sectional area of the respective specimen in the measuring range, E_{ABS}—Young's Modulus of additively manufactured polymer, E_{cF}—Young's Modulus of reinforcing fibers, E_{Epoxy}—Young's Modulus of matrix, φ_{FRP}—FVR of integrated cFRP, φ_{eff}—effective FVR of respective specimen in the measuring range, E_{FRP}—Young's Modulus of the integrated cFRP (contains cF and matrix phase).

A_{FRP} [mm²]	A_{eff} [mm²]	E_{ABS} [MPa]	E_{cF} [MPa]	E_{Epoxy} [MPa]	φ_{FRP}	φ_{eff}	E_{FRP} [MPa]	E_{theor} [MPa]
22.2	96.0	2400 acc. datasheet ABS-M30 stratasys	240,000 acc. datasheet HTS40 Toho Tenax	4300 acc. datasheet resin L + EPH161 R&G	41%	9.5%	100,937	25,174
					57%	13.2%	138,649	33,891

3.2. Mechanical Tests

3.2.1. Tensile Tests

The failure behavior of the reinforced specimens basically works according to the following principle: The force is applied or constrained on the additively manufactured basic structure, which has a lower stiffness than the cFRP. With an increasing load, the basic structure is elongated to a degree that induces high interlaminar shear stresses at the interface between the cFRP and the additively manufactured channel wall, which leads to the failure of the interface. Subsequently, the complete load is transferred to the basic structure. The failure of the basic structure occurs immediately after the failure of the interface. The damage pattern is basically identical for all reinforced specimens. The specimens fail either near the top or bottom restraint (Figure 8).

To investigate the failure behavior, an FEA model was created to simulate the tensile test (Figure 9). The FEA results, shown in Figure 10 and summarized in Figure 11, demonstrate that the contact force between the cFRP and the additively manufactured basic structure is at its maximum in the region of the restraint. In the region of maximum shear stress, the interface fails, and an initial crack is formed. With further progress, the crack expands, and the principal stress in the additively manufactured basic structure increases. As soon as the permissible stress in the additively manufactured basic structure is exceeded, complete failure occurs.

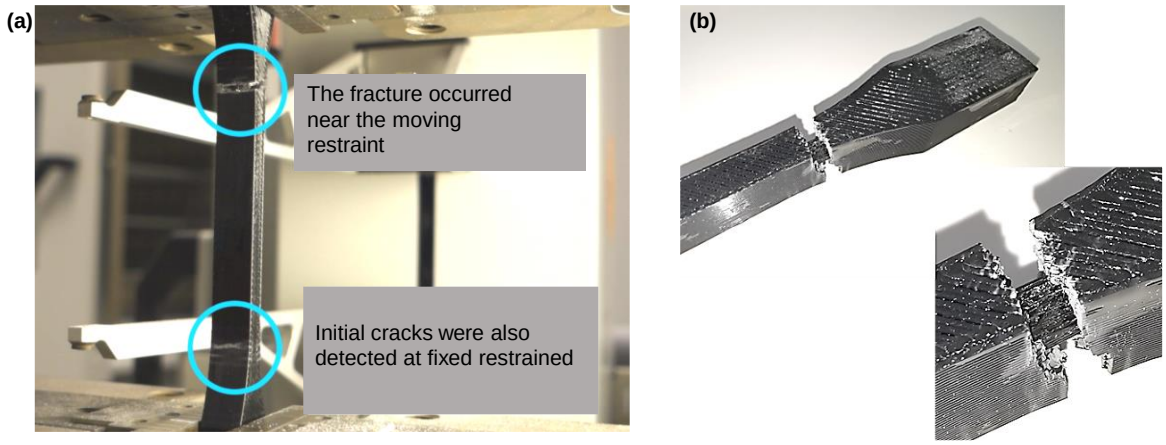

Figure 8. Restraining of specimen on tensile testing machine (**a**) and typical damage pattern (interface failure) on tensile specimens (**b**).

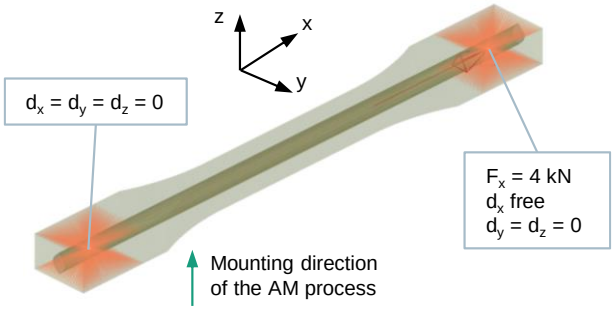

Figure 9. FEA model of a reinforced specimen with boundary conditions for the simulation of the tensile test. The model consists of an additively manufactured polymer basic structure and cFRP. The contact force is considered as failure criterion.

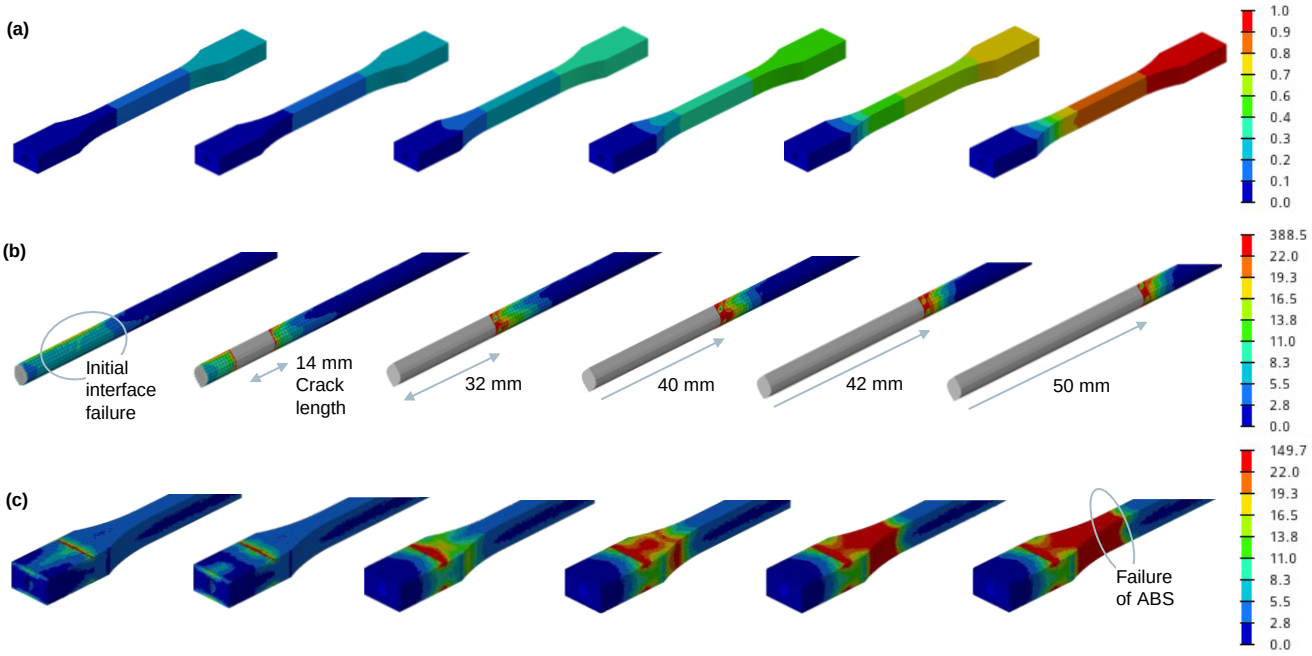

Figure 10. FEA results for (**a**) displacement in the x-direction [mm], (**b**) contact traction [N], and (**c**) principal major stress of additively manufactured basic structure [MPa] show initial crack and crack spreading at interface between cFRP and ABS.

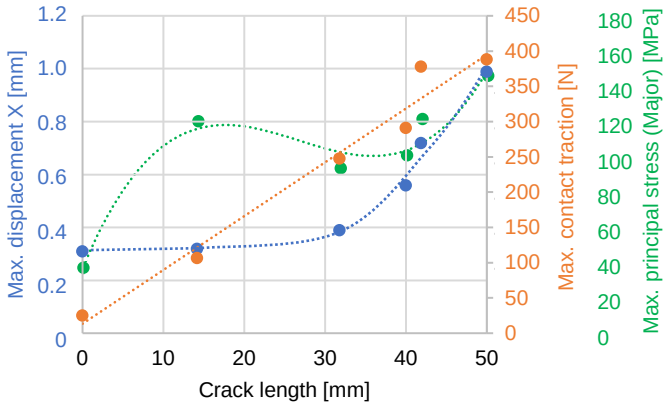

Figure 11. Summary of the FEA results according to the crack length.

A representative stress–strain curve of an unreinforced and a reinforced specimen is shown in Figure 12. The cFRP results in a significant increase in stiffness and strength. A detailed analysis of the reinforced specimen shows a drop in the stress–strain curve even before the maximum stress is reached (successive failure). This drop in the stress–strain curve indicates the initial failure. Parts of the matrix system detach from the channel wall, and the load is transferred to still-intact interface regions between the channel wall and the cFRP. Subsequently, the structure fails completely.

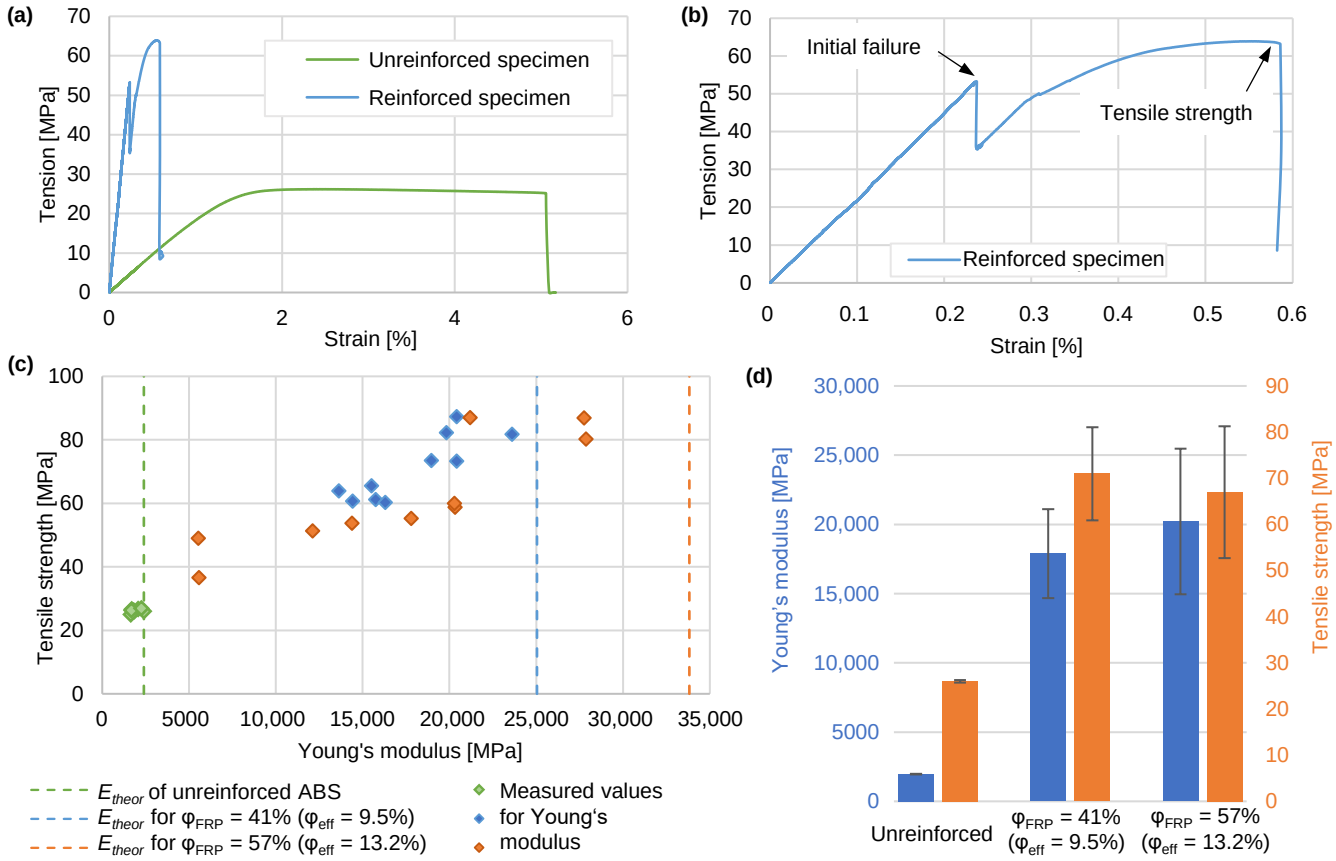

Figure 12. Evaluation of tensile tests. (**a**) Exemplary stress–strain curves on unreinforced and reinforced specimens. (**b**) Detailed stress–strain curve of exemplary reinforced specimen. (**c**) Individual measured and theoretically expected Young's moduli and tensile strengths. (**d**) Summary of the experimentally determined values with coefficients of variation.

Figure 12 and Table 4 show the results of the tensile tests. The Young's moduli of the unreinforced specimens determined experimentally are lower than those predicted according to the data sheet, which is a consequence of air inclusions due to the layer-by-layer deposition during the AM process (Figure 13). Consequently, the Young's moduli of the reinforced specimens are also lower than the previously theoretically determined values, with additional air inclusions in the matrix of the cFRP showing stiffness-reducing effects. Nevertheless, it is confirmed that the reinforced specimens exhibit significantly higher mechanical properties than the unreinforced specimens. The stress at initial failure of the reinforced specimens is 2.7 times higher than the tensile strength of the unreinforced specimens, and Young's modulus was increased by a factor of 9.1.

Table 4. Overview of the experimentally determined material properties of the unreinforced and reinforced additively manufactured structures with φ_{FRP}—FVR of cFRP, φ_{eff}—effective FVR, E—Young's modulus, σ_m—tensile strength at initial failure, E_r—flexural modulus, σ_f—flexural strength at initial failure, E_c—chord modulus, σ_c—compressive strength at initial failure, s—standard deviation, and V—coefficient of variation.

	Unreinforced Specimens		**Reinforced Specimens** φ_{FRP} **= 41%** (φ_{eff} **= 9.5%)**		**Reinforced Specimens** φ_{FRP} **= 57%** (φ_{eff} **= 13.2%)**	
Material constant						
Tension	E s V	σ_m s V	E s V	σ_m s V	E s V	σ_m s V
Flexure	E_r s V	σ_f s V	E_r s V	σ_f s V	E_r s V	σ_f s V
Compression	E_c s V	σ_c s V	E_c s V	σ_c s V	E_c s V	σ_c s V
Experimental results [MPa]						
Tension	1966 22 1.1%	26 0.3 1.2%	17,884 3217 18.0%	71 10.1 14.2%	20,212 5263 26.0%	67 14.3 21.3%
Flexure	1550 27 1.7%	50 0.4 0.8%	5300 196 3.7%	180 26 14.4%	5800 345 5.9%	200 33 16.5%
Compression	1750 33 1.9%	46 0.5 1.1%	8842 2380 26.9%	125 13 10.4%	- - -	- - -
Normalized mean values [-] *						
Tension	1	1	9.1	2.7	10.3	2.6
Flexure	1	1	3.4	3.6	3.7	4.0
Compression	1	1	5.1	2.7	-	-

* The normalized mean values E_{norm} and σ_{norm} are calculated according to Equation (8) or Equation (9).

The tensile strengths and Young's moduli of the reinforced specimens obtained in the tensile tests show a higher scatter than the unreinforced specimens, and the scatter of the test results is larger for an FVR of 57% than for an FVR of 41%. Figure 13 shows micrographs of one specimen with low mechanical properties and one specimen with high mechanical properties. Force transfer from the additively manufactured basic structure to the cFRP occurs via the matrix covering the channel wall. The degree of matrix covering the channel wall is of immense importance for a high-performance interface between the cFRP and the additively manufactured basic structure. Thus, the impregnation quality is

more important than the FVR because the interface between the channel wall and the fibers is the weakest point in the material composite.

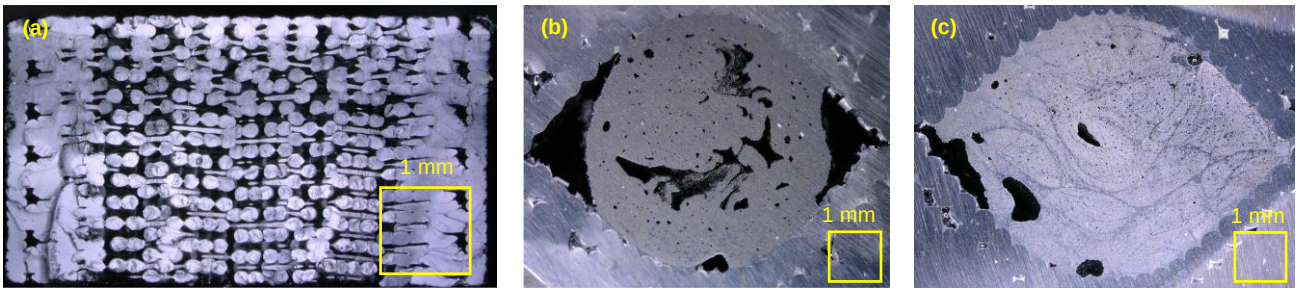

Figure 13. Micrographs of specimen (air inclusions in black). (**a**) Porosity due to layer-by-layer deposition of the polymer melt. (**b**) Reinforced specimen with low mechanical properties due to large air inclusions, especially at the channel wall. (**c**) Reinforced specimen with high mechanical properties due to good impregnation quality and good accumulation of the cFRP on channel wall.

3.2.2. Three-Point Bending Tests

The boundary conditions on the testing machine are shown in Figure 14. All specimens fail at the point of the maximum bending moment, which is located at the load application point. The specimens fail due to excessive deflection. In this case, the fibers carry almost the entire load. On the tensile-stressed side of the specimen, this is stretched to such an extent that a fiber fracture results, followed by a fracture of the additively manufactured basic structure. At the point of load application, an impression of the compression die (upper part of frame) was detected. Furthermore, as in the tensile tests, successive failure occurs. However, the reasons for this failure are not to be found in the failure of the interface, but in that of the fibers themselves.

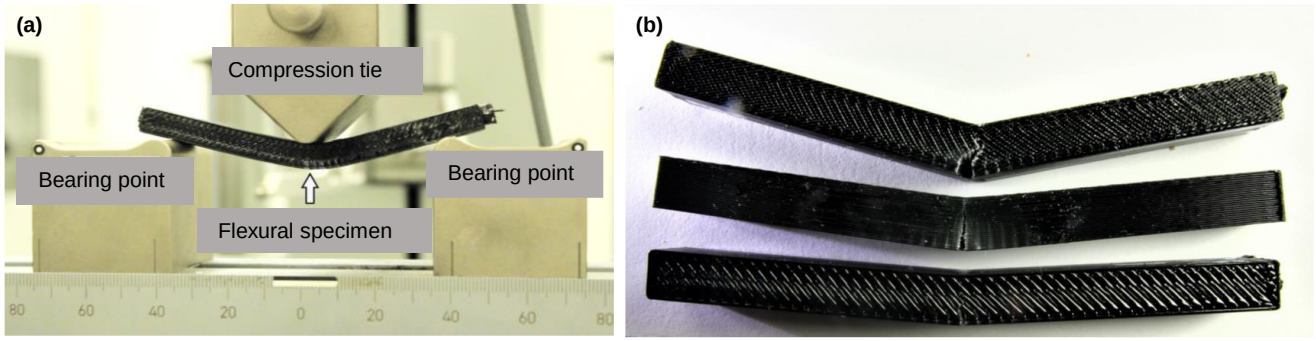

Figure 14. Three-point bending test of reinforced specimen (**a**) and details of tested specimens (**b**).

Figure 15 shows a representative stress–strain curve of an unreinforced and a reinforced specimen. In the case of the reinforced specimen, the stress increases approximately linearly until the initial failure is reached, and the stress drops abruptly to a lower level. The load is then transferred to fibers that are still intact and then fail completely (successive failure).

The individual results of the three-point bending tests are shown in Figure 15 and Table 4. Obviously, the cFRP leads to a significant increase in stiffness and strength. Compared with the unreinforced specimens, the flexural modulus of elasticity and the flexural strength were increased by factors of 5.1 and 2.7, respectively. As with the tensile tests, the results of the three-point bending tests scatter more with a high FVR than with a low FVR. Figure 16 shows two micrographs of a three-point bending specimen at two cross-sections. Air inclusion can be seen to occur at different locations. Coincidentally, if an air inclusion is located in the area of greatest stress, the performance of the composite structure will be negatively affected.

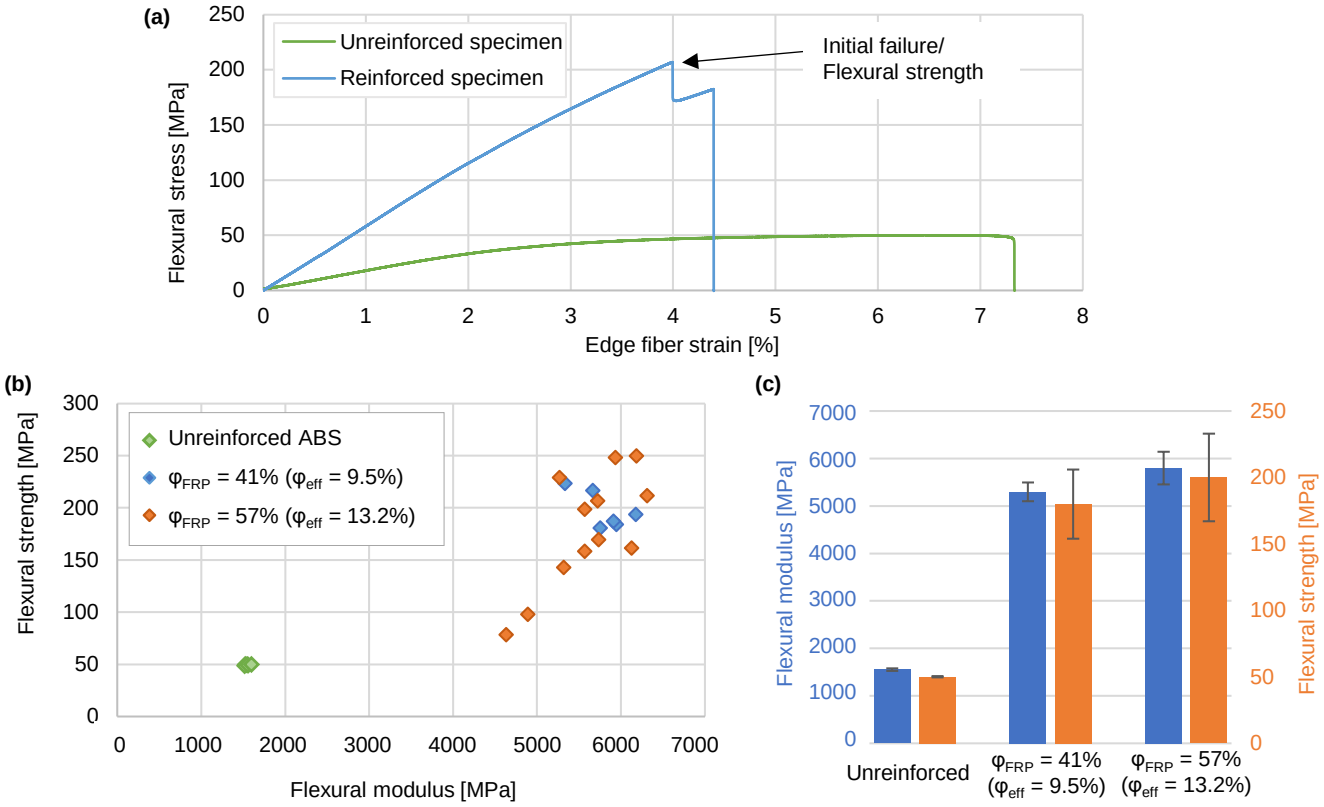

Figure 15. Evaluation of three-point bending tests. (**a**) Exemplary stress–strain curves on unreinforced and reinforced specimens. (**b**) Measured flexural moduli and flexural strengths. (**c**) Summary of the experimentally determined values with coefficients of variation.

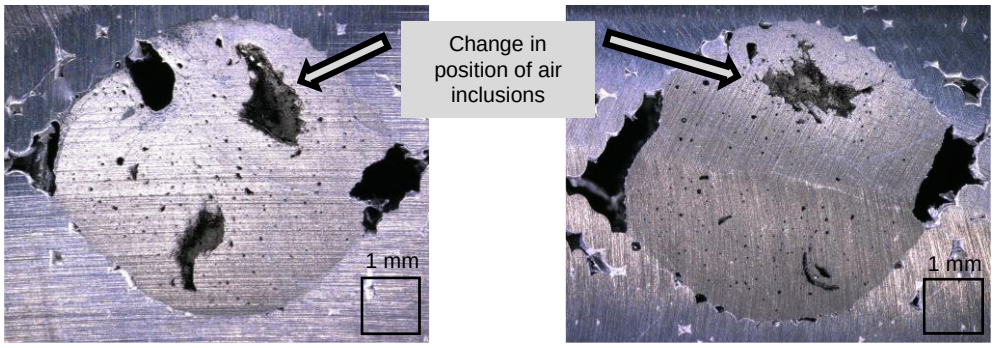

Figure 16. Micrographs of a flexure specimen at two cross-sections (air inclusions in black) show that air inclusions can occur at different locations along the specimen.

3.2.3. Compression Tests

Representative compressive stress–strain curves of an unreinforced or a reinforced specimen and a summary of the results of the compression tests are shown in Figure 17. While the unreinforced specimens showed significant compression, the reinforced specimens did not show any external damage. In the case of the reinforced specimen, the stress increases approximately linearly until the initial failure is reached, and the stress drops abruptly to a lower level. The introduction of the cFRP results in a factor of 3.4 in the chord modulus and a factor of 3.6 in the compressive strength. The mean values are summarized in Table 4.

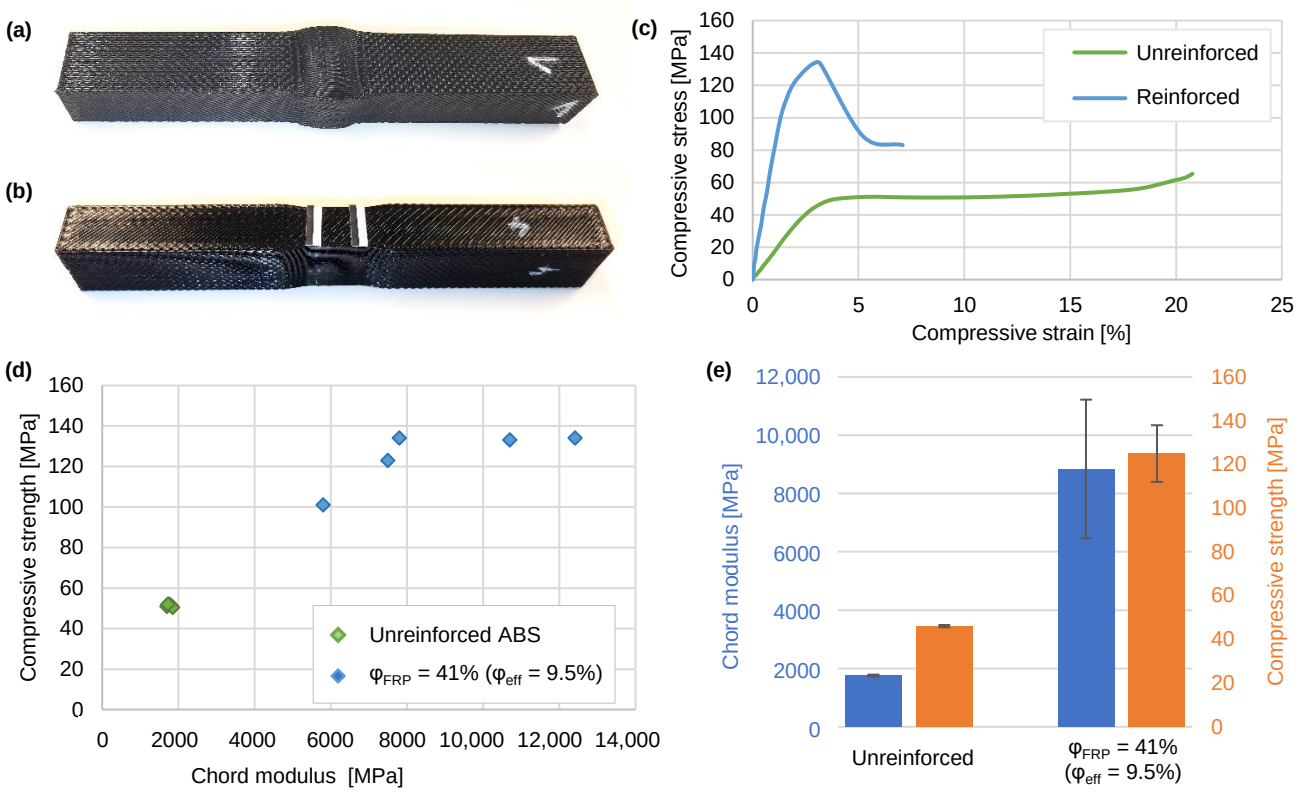

Figure 17. Unreinforced (**a**) and reinforced specimen (**b**) after compression test and evaluation of compression tests. (**c**) Exemplary stress–strain curves on unreinforced and reinforced specimens. (**d**) Chord moduli and compressive strengths. (**e**) Summary of the experimentally determined values with coefficients of variation.

3.2.4. Summary of the Mechanical Tests

Table 4 provides an overview of the experimentally determined material properties of the cFRP-reinforced and unreinforced additively manufactured polymer structures. In addition, the normalized mean values

$$E_{norm} = \frac{E_{reinforced}}{E_{unreinforced}} \tag{8}$$

and

$$\sigma_{norm} = \frac{\sigma_{reinforced}}{\sigma_{unreinforced}} \tag{9}$$

are provided, which indicate the stiffness and strength-influencing effect of the cFRP structure integrated into the additively manufactured basic structure (Figure 18). The mechanical tests for tension, compression, and flexure have shown that the mechanical properties of additively manufactured polymer structures are significantly increased by the integration of cFRP by means of the proposed method.

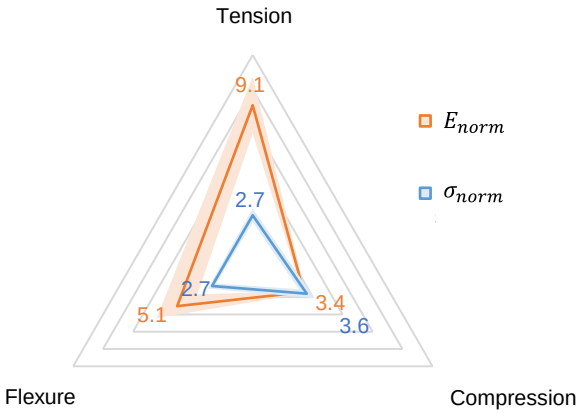

Figure 18. Normalized mean values of the mechanical tests at φ_{FRP} = 41% (φ_{eff} = 9.5%) demonstrate a significant increase in the mechanical properties, and coefficients of variation reveal the scattering of the measured values.

However, it should also be noted that the previously theoretically determined moduli (Table 3) are higher in comparison to the experimental results. These deviations can be caused by production-related effects (Figure 13), for example, air inclusions in the additively manufactured basic structure due to layer-by-layer deposition and in the integrated cFRP. Particularly, the interface between the cFRP and the additively manufactured basic structure at the channel wall offers potential for optimization. Further investigations must be carried out in further studies to utilize the full potential of the method presented.

3.2.5. Characteristic Mechanical Values of the Single Layers

Knowledge of the mechanical properties of the individual material components is essential for the dimensioning of composite structures. For this purpose, the properties of the unreinforced ABS determined by the shown experimental investigations can be used. However, the properties of the integrated cFRP cannot be measured directly. For the verification of the previously theoretically determined moduli (Table 3), the mechanical tests carried out were simulated using FEA using Ansys Workbench 2023. The contact between the additively manufactured basic structure and the cFRP at the channel wall is defined as bonded. It became clear that under the idealized assumption of the theoretical moduli, a strain occurs in the measuring range of the test specimens that is too low compared to the values measured in experiments. The deviation can be caused by production-related air inclusions in the cFRP or at the interface between the cFRP and the additively manufactured basic structure. Therefore, an adaption of the cFRP modulus was carried out in the FEA model, performed in a manual iteration process.

Figure 19 shows the corresponding FEA models and results of the tensile and compression tests, respectively, and a comparison with the measured strain. After iterative adjustment of the material parameters of the cFRP, a high level of correlation between the simulation and measurement results is achieved. In addition, the cFRP exhibits a bimodular behavior, i.e., the moduli under compressive and tensile stress significantly deviate from each other. Such a bimodular behavior can occur especially in fiber-reinforced materials with soft matrix [40,41]. During a flexure load, both tensile and compressive stresses occur. Therefore, a material model according to Ogden's 3rd order [42] was created for the FEA simulation of the flexural test, with which a bimodular behavior is replicated. The previously iteratively determined Young's modulus and chord modulus were transferred to the material model accordingly. A comparison of the numerical and experimental results of the three-point bending test shows a satisfactory correlation (Figure 19).

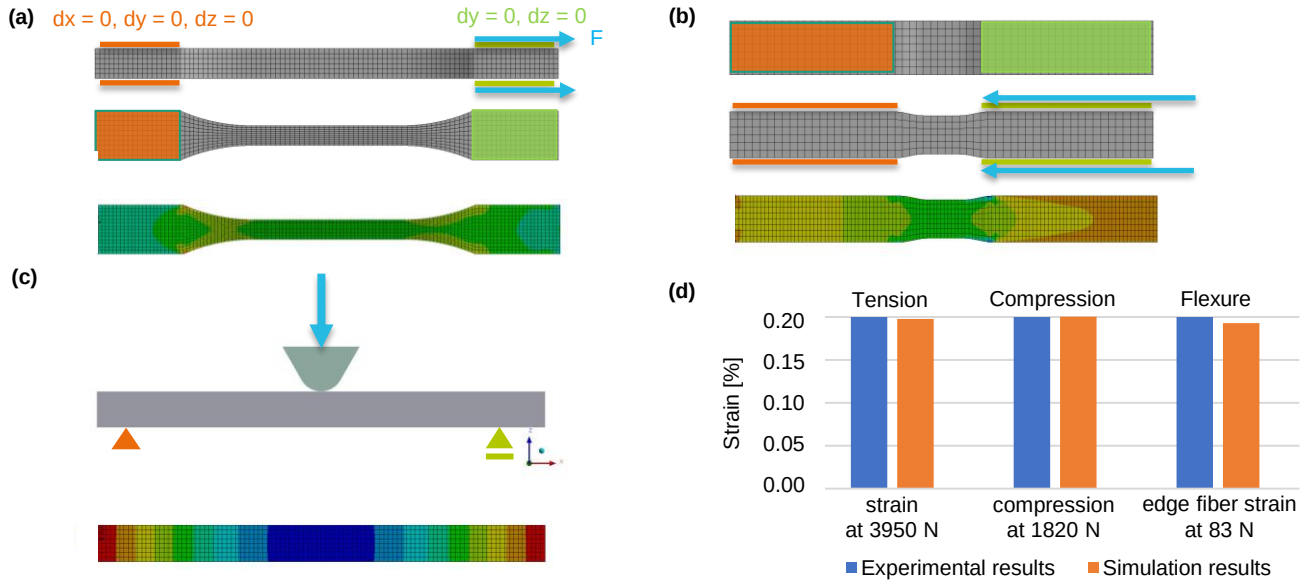

Figure 19. FEA model and simulation results (strain) with iteratively determined Young's modulus and chord modulus under tensile (**a**), compressive (**b**), and flexural loads (**c**). The comparison between the measured and simulated values shows a good correlation (**d**).

Table 5 summarizes the direction-dependent mechanical properties. The properties of the ABS are approximately quasi-isotropic. The properties of the cFRP are orthotropic and depend on the type of load (tension or compression).

Table 5. Overview of the iteratively determined material properties of unreinforced ABS and cFRP.

Tension Properties [MPa]				**ABS**	**1800 (All Directions)**		
	X	Y	Z	cFRP	X	Y	Z
X	E_x	G_{xy}	G_{xz}	X	80,000	9000	9000
Y	-	E_y	G_{yz}	Y	-	6000	8000
Z	-	-	E_z	Z	-	-	6000
Compression Properties [MPa]				**ABS**	**1800 (All Directions)**		
	X	Y	Z	cFRP	X	Y	Z
X	E_x	G_{xy}	G_{xz}	X	45,000	9000	9000
Y	-	E_y	G_{yz}	Y	-	6000	8000
Z	-	-	E_z	Z	-	-	6000
Poisson Constant [-]				**ABS**	**0.35 (All Directions)**		
	X	Y	Z	cFRP	X	Y	Z
X	-	ν_{xy}	ν_{xz}	X	-	0.2	0.2
Y	-	-	ν_{yz}	Y	-	-	0.35
Z	-	-	-	Z	-	-	-

3.3. General Design Guidelines

The mechanical tests confirmed that the two-step manufacturing method developed significantly increases the mechanical properties of additively manufactured polymer structures. The next objective is a demonstrative implementation of the manufacturing method. For this purpose, general design guidelines must be developed. For the preparation of design guidelines, it is necessary to investigate which restrictions exist for the design of the component-integrated channels. This includes the design of the cross-sectional area and the arrangement of the channels. Central issues are that the basic structure can be produced by means of AM and that the impregnated cF bundles can be pulled through the channels.

In AM using the FDM process, it should be noted that overhangs >45° can only be realized with an additional support structure. This is usually washed out with a specific solvent. The support structure inside the channel cannot be washed out, because the solvent does not circulate sufficiently strongly. Therefore, when using the FDM process, a drop-shaped channel geometry (Figure 20) is preferred. This has an overhang that is smaller than 45° and can be realized without a support structure. In addition, the minimum wall thickness should not be less than 2 mm. Experiments with a lower wall thickness have shown that a fracture in the additively manufactured basic structure near a channel radius can occur when the impregnated fibers are pulled through the channel.

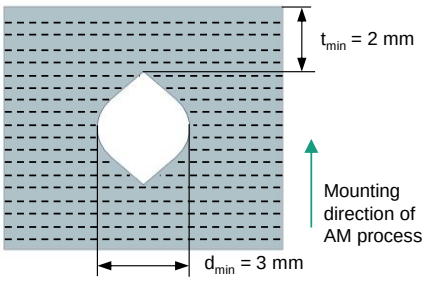

Figure 20. Design guideline for the channel cross-section in drop shape to avoid overhangs greater than 45° and a minimum wall thickness of 2 mm.

The channel length is a limiting design element in the manufacturing method developed. As the impregnated cF bundles are drawn in, friction occurs between the impregnated cF bundles and the channel wall of the additively manufactured basic structure. The frictional force to exceed increases with length of the channel. Tests were carried out with different channel lengths, and the traction force was measured. The test specimen and the results are shown in Figure 21. A maximum length of 800 mm is planned for the intended demonstrator, which was considered feasible for the experimental investigations carried out.

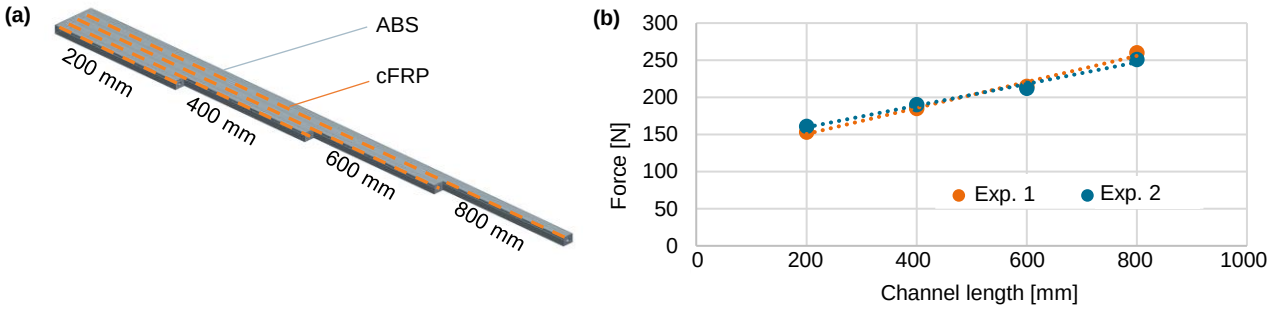

Figure 21. CAD model of specimens with different channel lengths (**a**) and traction force as a function of channel length (**b**).

The advantage of the presented method lies in the variable–axial design of the path of the cFRP. For this purpose, deflections of the fiber path must be realized. It was investigated whether a strong channel curvature, i.e., a small channel radius, has a negative influence on the impregnation quality and the interfacing with the component wall. For this purpose, a sample part was made with channels having different radii (Figure 22) and reinforced with cFRPs accordingly. Subsequently, samples were taken at the radius inlet and outlet, and quality control was carried out by means of micrographs. It is shown that at the minimum radius of 12.5 mm after channel curvature, the impregnation quality is similar to that before channel curvature. This channel radius is sufficient for the intended demonstrator.

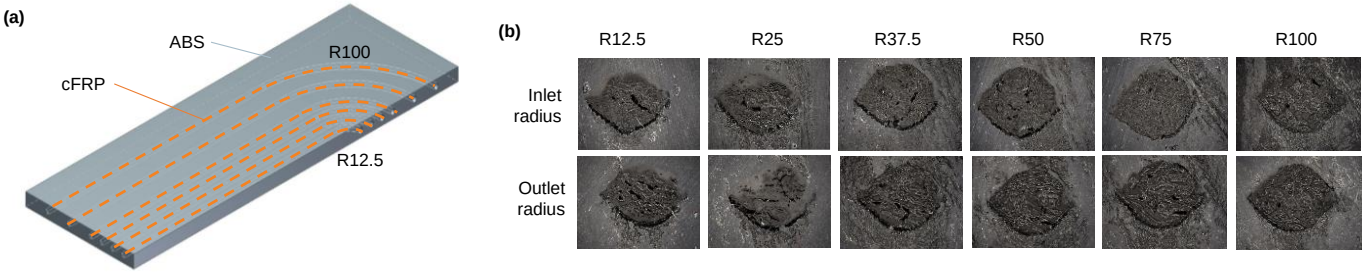

Figure 22. CAD model of the specimens with different channel radii (**a**) and micrographs for qualitative assessment of impregnation quality at radius inlet and outlet for different channel radii (**b**).

3.4. Structure Optimization and Design of Demonstrator Cantilevers

3.4.1. Topology Uptimization and Uiber Urientation

The progress of the combined optimization methods SKO and CAIO is shown in Figure 23. Visible is the topology optimization, where the elements with the minimum Young's modulus E_{min} = 6 MPa are hidden.

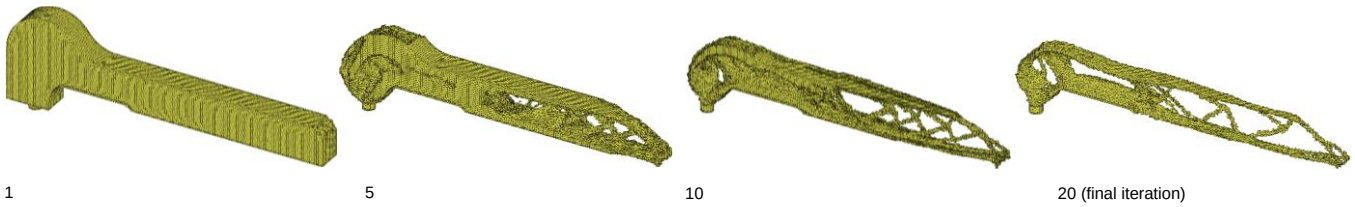

Figure 23. Development of topology optimization after selected iterations; the elements with the minimal Young's modulus E_{min} are hidden. The numbers given indicate the iteration number.

In addition to the consideration of orthotropic material properties, the integration of the CAIO approach allows for the element orientation to be adjusted in each iteration step. The compressive and tensile properties of the material are also taken into account and assigned accordingly in each case (Figure 24). This is necessary because the fiber-reinforced material used here has different tensile and compressive properties.

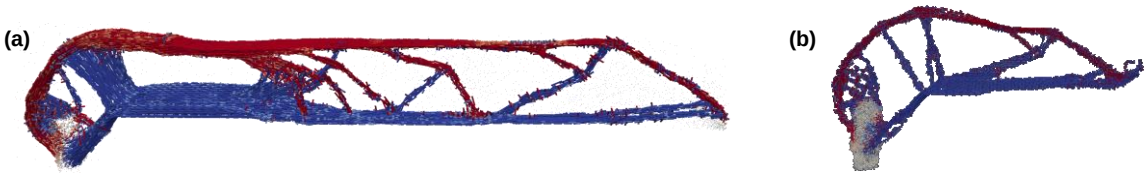

Figure 24. Optimization result of the combined fiber and topology optimization used to create the demonstrators. (**a**) Long version with 700 mm; (**b**) short version with 320 mm. The main stress directions are visualized in color (tension fibers in red and compression fibers in blue; visualization with Paraview, open source).

The development of a short (320 mm) and a long (700 mm) demonstrator shows different arrangements of supporting structures in the components.

3.4.2. Development of the Design Concept for the Fiber Channels

One special challenge within the method presented here is that there is currently no automated implementation option for all model requirements. In particular, the alignment of the fiber channels according to the determined design specifications must be emphasized here. Not only the minimum radius of 12.5 mm and the maximum length of 800 mm had to be taken into account. It was also necessary to minimize the number of radii in every single channel and to accept that the reinforced paths could not meet in a node, like in a space frame truss, but had to pass next to each other.

Consequently, the design proposal determined by the topology and fiber optimization must be abstracted and converted "manually", here, in CAD, into a wireframe model first (Figure 25). The cross-section for the fiber channels is created by thickening the wireframe model into a drop-shape form (Figure 26) and surrounded with matrix material (Figure 27). By this robust procedure, a basic geometry of the optimization results can be generated in a few steps and relatively short time and finally equipped with appropriate interfaces. For the professional use of the numerical tool, corresponding routines have to be further developed and implemented in the software packages.

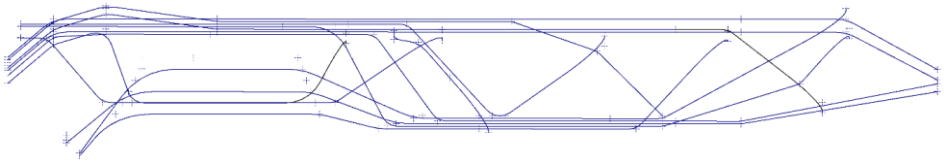

Figure 25. Creation of the CAD model for the demonstrator by generating a "wire model" consisting of lines and deflections.

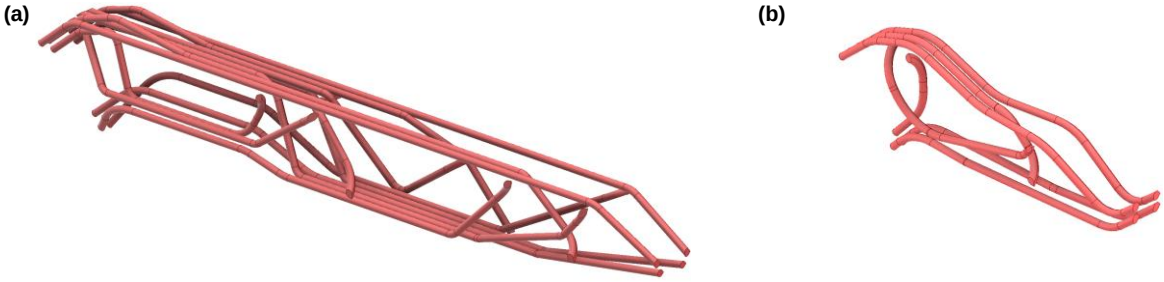

Figure 26. Realized fiber channels of the 700 mm demonstrator (**a**) as well as the 320 mm demonstrator (**b**); the channel diameter is 6.6 mm in each case.

Figure 27. Final CAD model of the 700 mm demonstrator (**a**) and the 320 mm demonstrator (**b**). Light red: input and output of the fiber channels into the construction.

3.4.3. Development and Preparation for Production of the Optimized Lightweight Structures

The final conception of the fiber channels (Figure 26) results in 13 fiber channels for the long version of the demonstrator; the short demonstrator is realized with 7 channels. Their channel diameters are 6.6 mm each. The cross-sectional shape of the fiber channels is approximately teardrop shaped to avoid overhangs greater than 45°. This means that no support structures are required within the channels during additive manufacturing. The matrix material is deposited around the fiber channels in the following process step (Figure 27).

Using the material components for the demonstrators as an example (ABS matrix: 1.05 g/cm^3, cFRP (FVR 41%): 1.4 g/cm^3), the mass of the 700 mm long model that can be extracted from the model simulation would be approx. 1164 g, and that of the 320 mm model would be approx. 349 g.

3.4.4. Numerical Validation of the Generated CAD Model

The numerical validation of the models takes into account both the matrix component and the fiber channels, i.e., their changed material characteristics compared to the properties

of the matrix material (see Sections 2.5.3 and 2.5.4). This allows for the compression- and tension-dominated regions within the channels to be calculated correctly.

Both models, the long version and the short one, are calculated and loaded in the same way with respect to both the material characteristics and the load cases (Figure 28). Table 6 provides the values from the validation for both demonstrator variants.

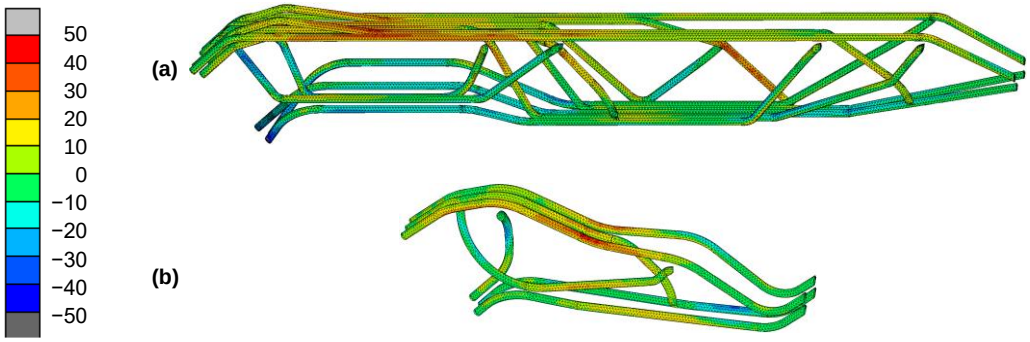

Figure 28. Major principal value of stress [MPa] in the fiber channels of the 700 mm demonstrator (**a**) and the 320 mm demonstrator (**b**). The surrounding ABS matrix is hidden to make the fiber channels visible.

Table 6. Results of the FEA validation.

	700 mm Demonstrator	320 mm Demonstrator
Max. tensile stress [MPa]	48	49
Max. compressive stress [MPa]	−66	−48
Max. total deformation [mm]	6.4	2.3
Max. lowering [mm]	6.2	1.5

The relevant yield strength for the fiber material is 57.9 MPa for tension and −127.8 MPa for compression. The major principal stress in the fiber channels does not exceed this limit, as shown in Figure 28, but due to the manual construction, not all areas are stressed evenly.

The analysis of the von Mises yield criterion in the demonstrator matrix shows that the stress is only slightly increased in the bearing area (Figure 29). The stresses determined in the FEA simulation are, in any case, below the yield strength of the material. These results indicate that the main load is carried by the fiber channels as intended.

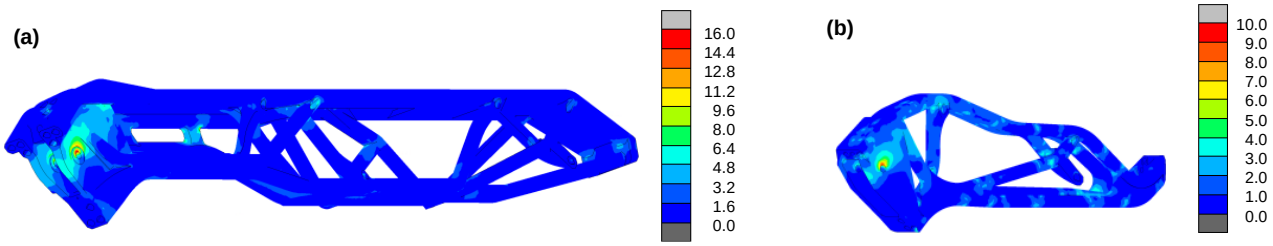

Figure 29. Von Mises yield criterion in the matrix of (**a**) the 700 mm demonstrator and (**b**) the 320 mm demonstrator (matrix material characteristics: isotropic, E = 1800 MPa, and ν = 0.35). The color reference is given in the unit MPa for both cases. To make the stress in the surrounding ABS matrix visible, the fiber channels are hidden. The large blue areas indicate that the matrix must endure little stress; only the bearing area shows slightly increased stress values.

3.5. Manufacturing and Validation of Demonstrator Cantilevers

The fabricated demonstrators are shown in Figure 30. In addition, a transparent structure was made to visualize the cF orientation. The demonstrator structure "long horizontal cantilever" was subjected to computed tomography (CT) to analyze the quality

of the inserted cFRP (Figure 31). This revealed that air inclusions systematically occur in the channel radii. When the impregnated cFs are pulled in, they contact the inner channel radius, so that there is no connection to the component wall of the additively manufactured basic structure at the outer channel radius. The experimental investigations carried out at the specimen level have shown that the interface between the cFRP and the additively manufactured basic structure is decisive for the load-bearing capacity of the overall structure. Consequently, in further studies, the focus should be on eliminating the systematic faults by taking suitable measures.

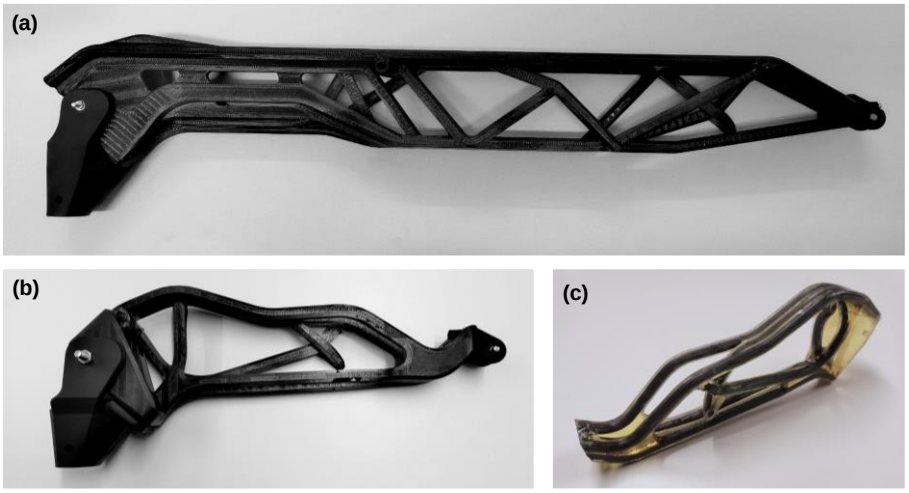

Figure 30. Demonstration structures manufactured using novel AM-cFRP method. (**a**) General view of long cantilever. (**b**) General view of short cantilever. (**c**) Short cantilever in transparent design shows fiber orientation.

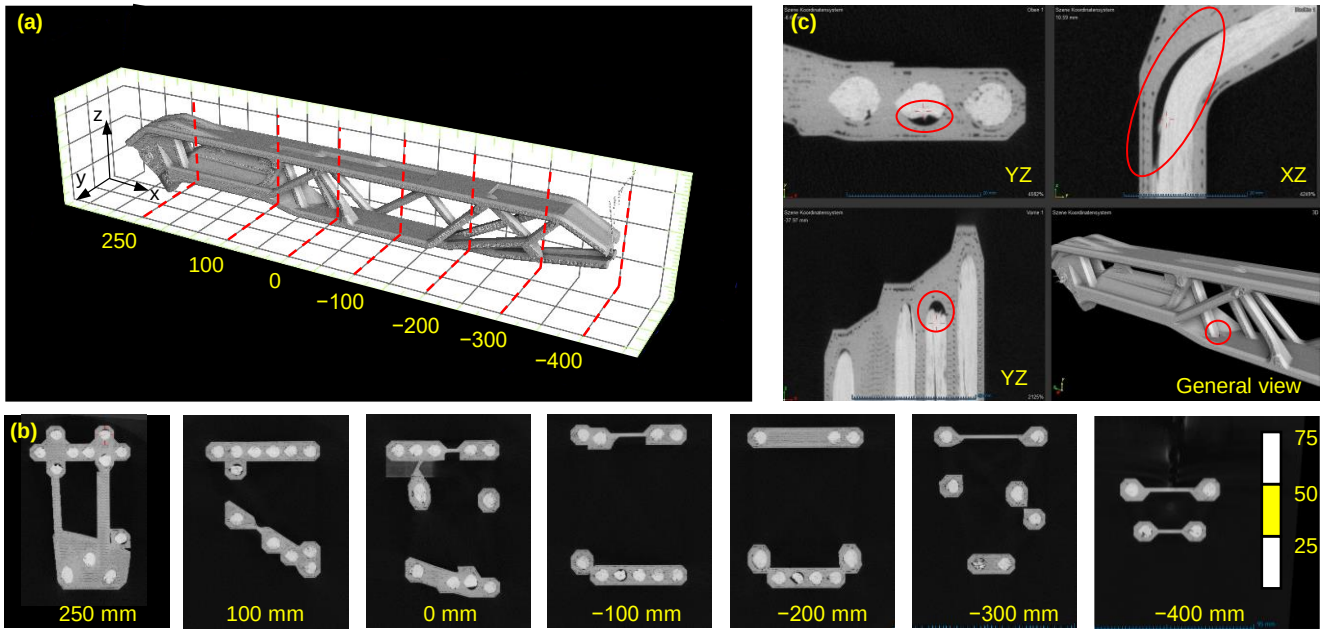

Figure 31. CT analysis of demonstrator cantilever. (**a**) General view with YZ cutting planes. (**b**) CT images on selected YZ section views. (**c**) Representative CT image at an exemplary deflection point with marked air inclusion in channel radius.

The developed cantilevers were implemented and validated in a functional demonstrator of an exoskeleton (Figure 32). For this purpose, corresponding interfaces of the cantilever were designed to enable a connection with the existing exoskeleton.

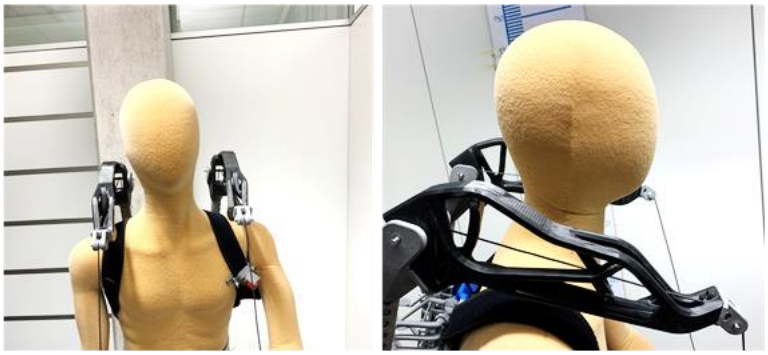

Figure 32. Integration of the developed (short) cantilevers into an existing test exoskeleton.

The cantilevers realized using the novel method were compared with existing unreinforced additively manufactured cantilevers. The newly developed load-bearing structures are significantly superior to the previously used ones. While the deflections of the unreinforced cantilevers were too large and thus unsuitable for the intended application, the deflections of the cantilevers have been considerably reduced to a suitable value by using the novel method. The results of the demonstrator validation proved the feasibility of the novel method for reinforcing additively manufactured polymer structures with component-integrated cFRPs.

4. Discussion

Compared to established cF-AM methods, the main advantage of the developed method is primarily the possibility of arranging reinforcing fibers variably–axially along the principal stress lines and independently from the AM mounting direction. The studies carried out have clearly demonstrated the feasibility of the method.

To assess the potential of the method, the results of the study were benchmarked against conventional FRP technologies, short-fiber AM and cF-AM methods (Figure 33). Especially compared to other cF-AM methods, the novel method is still in a lower performance range in terms of tensile strength in the fiber direction. A current overview regarding the mechanical properties of various cF-AM methods is provided by Safari et al. [21]. Studies presenting cF-AM methods with high tensile strength are, for example, [43–53].

The interface of the cFRP structure at the channel wall of the additively manufactured basic structure has emerged as a central, significant influencing factor. From the specimen and demonstrator validation, there is potential for optimizing the method in further studies. The following hypotheses are derived from the findings of the study:

(1) The interlaminar strength is significantly influenced by the amount of surface area covered with matrix material on the component-integrated channel wall. An adapted channel geometry with an increased surface will consequently result in an improvement in interlaminar strength.
(2) The interlaminar strength is essentially determined by the adhesive interaction between the matrix material and the polymer used for AM of the basic structure. A targeted modification or substitution of the material components will therefore result in an increase in the interlaminar strength.
(3) The matrix material must ideally cover the channel surface completely to create the conditions for a maximum number of adhesion points in the bonding zone. Consequently, the increase in impregnation quality will be associated with an improvement in the interlaminar strength.

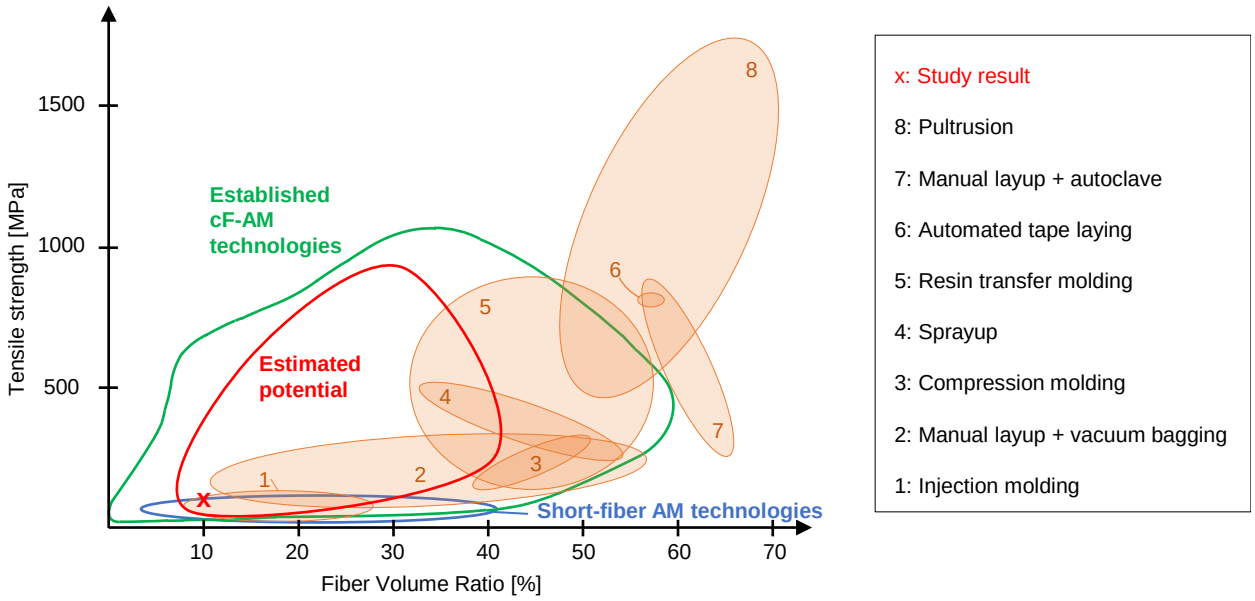

Figure 33. FVR and tensile strengths achievable with conventional FRP processes, short-fiber-reinforced AM, and established cF-reinforced AM methods (inspired by [21,23]). Assessment of the study results shows that the novel method is currently still at a lower performance level. However, a significant increase is expected due to an improvement in interlaminar strength.

5. Conclusions

A state-of-the-art analysis showed that processes integrating cFs in AM are very efficient in terms of their mechanical properties and can be comparable to established FRP processes. However, based on the evaluation of existing cF-AM methods, it was also determined that cF integration during the AM process can partially exclude applications as soon as an in-plane arrangement of the cF is not sufficient:

(1) The deficit of existing cF-AM methods regarding the high degree of structural anisotropy could be solved with the presented method, in which the cF integration is decoupled from the AM process.
(2) The method allows for a variable–axial arrangement of cFs independently of the AM mounting direction.
(3) The investigations at the specimen level evidenced a significant increase in mechanical properties regarding its tensile, compressive, and flexural properties compared with unreinforced specimens.
(4) Design restrictions in the execution of the component-integrated channels regarding the channel geometry, length, and radius were demonstrated based on sample structures. Design guidelines were derived.
(5) The proof of concept was provided by means of demonstrators.
(6) The numerical tool, which combines two methods of structural optimization, is well suited for the design of additively manufactured polymer structures with variable–axial cF reinforcement.
(7) As a result of the load-adjusted integration of cFRP in additively manufactured polymer structures, a significantly higher load-bearing capacity, an increased degree of lightweight construction, and a reduced material usage were realized compared with unreinforced additively manufactured polymer structures.
(8) The method is predestined to realize geometrically complex lightweight structures in single-part and small-series production.
(9) Compared to other cf-AM methods, the novel method is still in a lower performance range in terms of tensile strength in the fiber direction. Promising approaches to further improve the mechanical properties and reproducibility were presented. These

relate to the modification of the material composition, channel geometry, and impregnation quality.

Author Contributions: Conceptualization, S.M. (Sven Meißner); methodology—testing, S.M. (Sven Meißner) and J.K.; methodology—optimization, H.I. and S.L.; methodology—application scenario, O.E. and H.K.; validation, S.M. (Sven Meißner), H.I. and O.E.; investigation, J.K. and H.I.; writing—original draft preparation, S.M. (Sven Meißner); writing—review and editing, H.I., S.L., A.K., S.S., S.M. (Sascha Müller), A.S. and L.K.; visualization, D.K.; project administration, S.M. (Sven Meißner), A.K. and H.K.; funding acquisition, S.M. (Sven Meißner), A.K. and H.K. All authors have read and agreed to the published version of the manuscript.

Funding: This research was funded by the German Federal Ministry of Education and Research (BMBF) as part of the project "AM-Reinforce", grant numbers 02P20E160, 02P20E161, and 02P20E162.

Data Availability Statement: Data are contained within the article.

Conflicts of Interest: Oliver Eberhardt and Harald Kuolt were employed by the company J. Schmalz GmbH. The remaining authors declare that the research was conducted in the absence of any commercial or financial relationships that could be construed as a potential conflict of interest.

References

1. Wohlers, T.T.; Campbell, I.; Diegel, O.; Huff, R.; Kowen, J. *Wohlers Report 2022: 3D Printing and Additive Manufacturing Global State of the Industry*; Wohlers Associates: Fort Collins, CO, USA, 2022; ISBN 9780991333295.
2. Rehnberg, M.; Ponte, S. From smiling to smirking? 3D printing, upgrading and the restructuring of global value chains. *Glob. Netw.* **2018**, *18*, 57–80. [CrossRef]
3. Kuncius, T.; Rimašauskas, M.; Rimašauskienė, R. Interlayer Adhesion Analysis of 3D-Printed Continuous Carbon Fibre-Reinforced Composites. *Polymers* **2021**, *13*, 1653. [CrossRef] [PubMed]
4. Kristiawan, R.B.; Imaduddin, F.; Ariawan, D.; Ubaidillah; Arifin, Z. A review on the fused deposition modeling (FDM) 3D printing: Filament processing, materials, and printing parameters. *Open Eng.* **2021**, *11*, 639–649. [CrossRef]
5. Syrlybayev, D.; Zharylkassyn, B.; Seisekulova, A.; Akhmetov, M.; Perveen, A.; Talamona, D. Optimisation of Strength Properties of FDM Printed Parts—A Critical Review. *Polymers* **2021**, *13*, 1587. [CrossRef] [PubMed]
6. Thumsorn, S.; Prasong, W.; Kurose, T.; Ishigami, A.; Kobayashi, Y.; Ito, H. Rheological Behavior and Dynamic Mechanical Properties for Interpretation of Layer Adhesion in FDM 3D Printing. *Polymers* **2022**, *14*, 2721. [CrossRef] [PubMed]
7. Wach, R.A.; Wolszczak, P.; Adamus-Wlodarczyk, A. Enhancement of Mechanical Properties of FDM-PLA Parts via Thermal Annealing. *Macromol. Mater. Eng.* **2018**, *303*, 1800169. [CrossRef]
8. Spoerk, M.; Gonzalez-Gutierrez, J.; Sapkota, J.; Schuschnigg, S.; Holzer, C. Effect of the printing bed temperature on the adhesion of parts produced by fused filament fabrication. *Plast. Rubber Compos.* **2018**, *47*, 17–24. [CrossRef]
9. Popescu, D.; Zapciu, A.; Amza, C.; Baciu, F.; Marinescu, R. FDM process parameters influence over the mechanical properties of polymer specimens: A review. *Polym. Test.* **2018**, *69*, 157–166. [CrossRef]
10. Mohamed, O.A.; Masood, S.H.; Bhowmik, J.L. Optimization of fused deposition modeling process parameters: A review of current research and future prospects. *Adv. Manuf.* **2015**, *3*, 42–53. [CrossRef]
11. Li, H.; Wang, T.; Sun, J.; Yu, Z. The effect of process parameters in fused deposition modelling on bonding degree and mechanical properties. *Rapid Prototyp. J.* **2018**, *24*, 80–92. [CrossRef]
12. Wickramasinghe, S.; Do, T.; Tran, P. FDM-Based 3D Printing of Polymer and Associated Composite: A Review on Mechanical Properties, Defects and Treatments. *Polymers* **2020**, *12*, 1529. [CrossRef] [PubMed]
13. Chen, H.; Zhu, W.; Tang, H.; Yan, W. Oriented structure of short fiber reinforced polymer composites processed by selective laser sintering: The role of powder-spreading process. *Int. J. Mach. Tools Manuf.* **2021**, *163*, 103703. [CrossRef]
14. van de Werken, N.; Tekinalp, H.; Khanbolouki, P.; Ozcan, S.; Williams, A.; Tehrani, M. Additively manufactured carbon fiber-reinforced composites: State of the art and perspective. *Addit. Manuf.* **2020**, *31*, 100962. [CrossRef]
15. Salazar, A.; Rico, A.; Rodríguez, J.; Segurado Escudero, J.; Seltzer, R.; La Martin de Escalera Cutillas, F. Fatigue crack growth of SLS polyamide 12: Effect of reinforcement and temperature. *Compos. Part B Eng.* **2014**, *59*, 285–292. [CrossRef]
16. Badini, C.; Padovano, E.; de Camillis, R.; Lambertini, V.G.; Pietroluongo, M. Preferred orientation of chopped fibers in polymer-based composites processed by selective laser sintering and fused deposition modeling: Effects on mechanical properties. *J. Appl. Polym. Sci.* **2020**, *137*, 49152. [CrossRef]
17. Dickson, A.N.; Abourayana, H.M.; Dowling, D.P. 3D Printing of Fibre-Reinforced Thermoplastic Composites Using Fused Filament Fabrication—A Review. *Polymers* **2020**, *12*, 2188. [CrossRef] [PubMed]
18. Ahmadifar, M.; Benfriha, K.; Shirinbayan, M.; Tcharkhtchi, A. Additive Manufacturing of Polymer-Based Composites Using Fused Filament Fabrication (FFF): A Review. *Appl. Compos. Mater.* **2021**, *28*, 1335–1380. [CrossRef]
19. Pratama, J.; Cahyono, S.I.; Suyitno, S.; Muflikhun, M.A.; Salim, U.A.; Mahardika, M.; Arifvianto, B. A Review on Reinforcement Methods for Polymeric Materials Processed Using Fused Filament Fabrication (FFF). *Polymers* **2021**, *13*, 4022. [CrossRef] [PubMed]

20. Sculpteo—The State of 3D Printing 2021. Available online: https://www.sculpteo.com/en/ebooks/state-of-3d-printing-report-2021/ (accessed on 11 August 2023).
21. Safari, F.; Kami, A.; Abedini, V. 3D printing of continuous fiber reinforced composites: A review of the processing, pre- and post-processing effects on mechanical properties. *Polym. Polym. Compos.* **2022**, *30*, 096739112210987. [CrossRef]
22. Mashayekhi, F.; Bardon, J.; Berthé, V.; Perrin, H.; Westermann, S.; Addiego, F. Fused Filament Fabrication of Polymers and Continuous Fiber-Reinforced Polymer Composites: Advances in Structure Optimization and Health Monitoring. *Polymers* **2021**, *13*, 789. [CrossRef] [PubMed]
23. Goh, G.D.; Yap, Y.L.; Agarwala, S.; Yeong, W.Y. Recent Progress in Additive Manufacturing of Fiber Reinforced Polymer Composite. *Adv. Mater. Technol.* **2019**, *4*, 1800271. [CrossRef]
24. Pandelidi, C.; Bateman, S.; Piegert, S.; Hoehner, R.; Kelbassa, I.; Brandt, M. The technology of continuous fibre-reinforced polymers: A review on extrusion additive manufacturing methods. *Int. J. Adv. Manuf. Technol.* **2021**, *113*, 3057–3077. [CrossRef]
25. Zhuo, P.; Li, S.; Ashcroft, I.A.; Jones, A.I. Material extrusion additive manufacturing of continuous fibre reinforced polymer matrix composites: A review and outlook. *Compos. Part B Eng.* **2021**, *224*, 109143. [CrossRef]
26. Struzziero, G.; Barbezat, M.; Skordos, A.A. Consolidation of continuous fibre reinforced composites in additive processes: A review. *Addit. Manuf.* **2021**, *48*, 102458. [CrossRef]
27. Spickenheuer, A. Zur Fertigungsgerechten Auslegung von Faser-Kunststoff-Verbundbauteilen für den Extremen Leichtbau auf Basis des Variabelaxialen Fadenablageverfahrens Tailored Fiber Placement. Ph.D. Thesis, Technische Universität Dresden, Dresden, Germany, 2014.
28. Holzinger, M.; Blase, J.; Reinhardt, A.; Kroll, L. New additive manufacturing technology for fibre-reinforced plastics in skeleton structure. *J. Reinf. Plast. Compos.* **2018**, *37*, 1246–1254. [CrossRef]
29. Hirsch, P.; Scholz, S.; Borowitza, B.; Vyhnal, M.; Schlimper, R.; Zscheyge, M.; Kotera, O.; Stipkova, M.; Scholz, S. Processing and Analysis of Hybrid Fiber-Reinforced Polyamide Composite Structures Made by Fused Granular Fabrication and Automated Tape Laying. *J. Manuf. Mater. Process.* **2024**, *8*, 25. [CrossRef]
30. Habenicht, G. *Kleben*; Springer: Berlin/Heidelberg, Germany, 2009; ISBN 978-3-540-85264-3.
31. *ISO 527-4:2023*; Plastics—Determination of Tensile Properties—Part 4: Test Conditions for Isotropic and Orthotropic Fibre-Reinforced Plastic Composites. International Organization for Standardization (ISO): Geneva, Switzerland, 2023.
32. *ISO 14125:1998*; Fibre-Reinforced Plastic Composites—Determination of Flexural Properties. International Organization for Standardization (ISO): Geneva, Switzerland, 1998.
33. *ISO 14126:2023*; Fibre-Reinforced Plastic Composites—Determination of Compressive Properties In the in-Plane Direction. International Organization for Standardization (ISO): Geneva, Switzerland, 2023.
34. *DIN EN ISO 527-2-2012*; Plastics—Determination of Tensile Properties—Part 2: Test Conditions for Moulding and Extrusion Plastics. Beuth Verlag GmbH: Berlin, Germany, 2012.
35. J. Schmalz GmbH. 2023. Available online: https://www.schmalz.com/de-de/ (accessed on 12 December 2023).
36. Hamm, C. *Evolution of Lightweight Structures*; Springer: Dordrecht, The Netherlands, 2015; ISBN 978-94-017-9397-1.
37. Mattheck, C. Engineering Components grow like trees. *Mater. Werkst.* **1990**, *21*, 143–168. [CrossRef]
38. Baumgartner, A.; Harzheim, L.; Mattheck, C. SKO (soft kill option): The biological way to find an optimum structure topology. *Int. J. Fatigue* **1992**, *14*, 387–393. [CrossRef]
39. Kriechbaum, R. Ein Verfahren zur Optimierung der Faserverläufe in Verbundwerkstoffen durch Minimierung der Schubspannungen nach Vorbildern der Natur. Ph.D. Thesis, Universität Karlsruhe, Karlsruhe, Germany, 1994.
40. Zhang, L.; Zhang, H.W.; Wu, J.; Yan, B. A stabilized complementarity formulation for nonlinear analysis of 3D bimodular materials. *Acta Mech. Sin.* **2016**, *32*, 481–490. [CrossRef]
41. Sacco, E.; Reddy, J.N. A Constitutive Model for Bimodular Materials with an Application to Plate Bending. *J. Appl. Mech.* **1992**, *59*, 220–221. [CrossRef]
42. Ogden, R.W.; Ogden, R.W. *Non-Linear Elastic Deformations*; 1. Publ., Unabridged and Corr. Republ.; Dover Publications: Mineola, NY, USA, 1997; ISBN 0486696480.
43. Ueda, M.; Kishimoto, S.; Yamawaki, M.; Matsuzaki, R.; Todoroki, A.; Hirano, Y.; Le Duigou, A. 3D compaction printing of a continuous carbon fiber reinforced thermoplastic. *Compos. Part A Appl. Sci. Manuf.* **2020**, *137*, 105985. [CrossRef]
44. Giannakis, E.; Koidis, C.; Kyratsis, P.; Tzetzis, D. Static and fatigue properties of 3d printed continuous continuous carbon fiber nylon composites. *Int. J. Mod. Manuf. Technol.* **2019**, *XI*, 69–76.
45. Hao, W.; Liu, Y.; Zhou, H.; Chen, H.; Fang, D. Preparation and characterization of 3D printed continuous carbon fiber reinforced thermosetting composites. *Polym. Test.* **2018**, *65*, 29–34. [CrossRef]
46. Hou, Z.; Tian, X.; Zheng, Z.; Zhang, J.; Zhe, L.; Li, D.; Malakhov, A.V.; Polilov, A.N. A constitutive model for 3D printed continuous fiber reinforced composite structures with variable fiber content. *Compos. Part B Eng.* **2020**, *189*, 107893. [CrossRef]
47. Iragi, M.; Pascual-González, C.; Esnaola, A.; Lopes, C.S.; Aretxabaleta, L. Ply and interlaminar behaviours of 3D printed continuous carbon fibre-reinforced thermoplastic laminates; effects of processing conditions and microstructure. *Addit. Manuf.* **2019**, *30*, 100884. [CrossRef]
48. Pyl, L.; Kalteremidou, K.-A.; van Hemelrijck, D. Exploration of specimen geometry and tab configuration for tensile testing exploiting the potential of 3D printing freeform shape continuous carbon fibre-reinforced nylon matrix composites. *Polym. Test.* **2018**, *71*, 318–328. [CrossRef]

49. Todoroki, A.; Oasada, T.; Mizutani, Y.; Suzuki, Y.; Ueda, M.; Matsuzaki, R.; Hirano, Y. Tensile property evaluations of 3D printed continuous carbon fiber reinforced thermoplastic composites. *Adv. Compos. Mater.* **2020**, *29*, 147–162. [CrossRef]
50. Zhang, J.; Zhou, Z.; Zhang, F.; Tan, Y.; Tu, Y.; Yang, B. Performance of 3D-Printed Continuous-Carbon-Fiber-Reinforced Plastics with Pressure. *Materials* **2020**, *13*, 471. [CrossRef]
51. Goh, G.D.; Dikshit, V.; Nagalingam, A.P.; Goh, G.L.; Agarwala, S.; Sing, S.L.; Wei, J.; Yeong, W.Y. Characterization of mechanical properties and fracture mode of additively manufactured carbon fiber and glass fiber reinforced thermoplastics. *Mater. Des.* **2018**, *137*, 79–89. [CrossRef]
52. Ghebretinsae, F.; Mikkelsen, O.; Akessa, A.D. Strength analysis of 3D printed carbon fibre reinforced thermoplastic using experimental and numerical methods. *IOP Conf. Ser. Mater. Sci. Eng.* **2019**, *700*, 012024. [CrossRef]
53. Dutra, T.A.; Ferreira, R.T.L.; Resende, H.B.; Guimarães, A. Mechanical characterization and asymptotic homogenization of 3D-printed continuous carbon fiber-reinforced thermoplastic. *J. Braz. Soc. Mech. Sci. Eng.* **2019**, *41*, 133. [CrossRef]